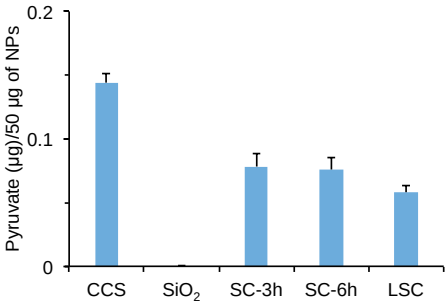

Supplementary Figure 1. The presence of pyruvate in LSC nanoparticles. The pyruvate content in CCS nanoparticles, pure silica (SiO_2) nanoparticles, SC nanoparticles made with 3 and 6 h of reaction, and LSC nanoparticles. The assay interacts mainly with the nanoparticle surface. A total of 50 μg of nanoparticles (NPs) were used in the detection. Error bars represent s.d. (n = 3).

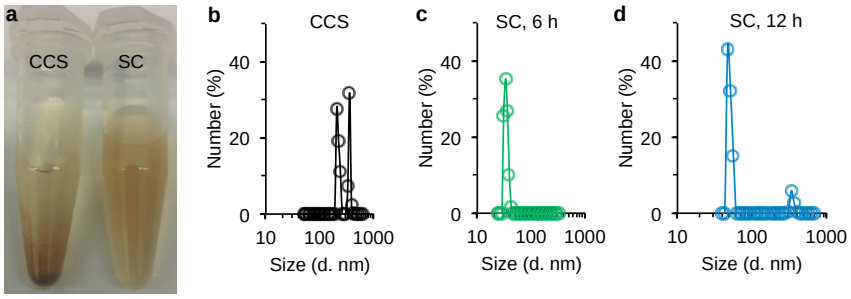

Supplementary Figure 2. Stability and size distribution of colloidal carbon sphere and silica-carbon nanoparticles. (**a**), Photograph of the colloidal carbon sphere (CCS) and silica-carbon (SC) nanoparticles in deionized water (2 mg ml^{-1}). The SC nanoparticles can be well dispersed in deionized water while the CCS nanoparticles form aggregates and sediment at the bottom of the tube. (**b**), Size distribution of CCS nanoparticles showing two major peaks as a result of forming large aggregates in deionized water. (**c-d**), Size distribution of SC nanoparticles made with reaction times of 6 h (c) and 12 h (d), showing the SC nanoparticles made with the reaction time of 12 h are bigger than the ones made with 6 h. A minor peak is also observable for the size distribution of the SC nanoparticles made with 12 h of reaction, suggesting some of the nanoparticles also form aggregates.

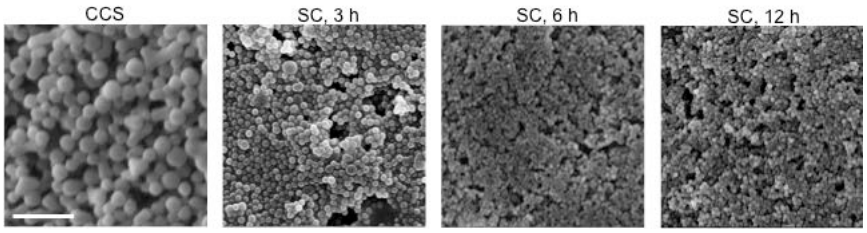

Supplementary Figure 3. Characterization of nanoparticles with scanning electron microscopy. Scanning electron microscopy (SEM) images of the CCS and SC nanoparticles synthesized with different reaction times, showing SC nanoparticles of ~35 nm with a homogeneous size distribution can be obtained after 6 h of reaction. Scale bars: 1 μm.

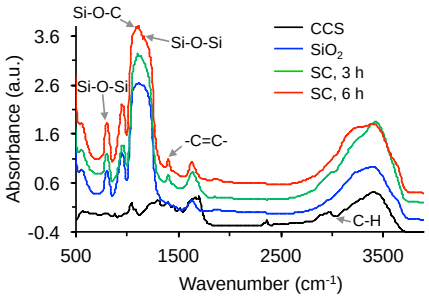

Supplementary Figure 4. FTIR data showing successful synthesis of SC nanoparticles. Fourier transform infrared (FTIR) spectra of CCS nanoparticles, pure silica (SiO_2) nanoparticles, and SC nanoparticles made with 3 h and 6 h of reaction showing (1), the presence of CCS (indicated by the C=C bond at 1396 cm^{-1}) and silica (indicated by the Si-O-Si bond at 788 cm^{-1}) in the CS nanoparticles and (2), the reaction between silica and CCS indicated by the Si-O-C bond at 1070 cm^{-1} according to previous study (Jeong et al. *Angew. Chem. Int. Ed*. 2009, 48, 5296-5299).

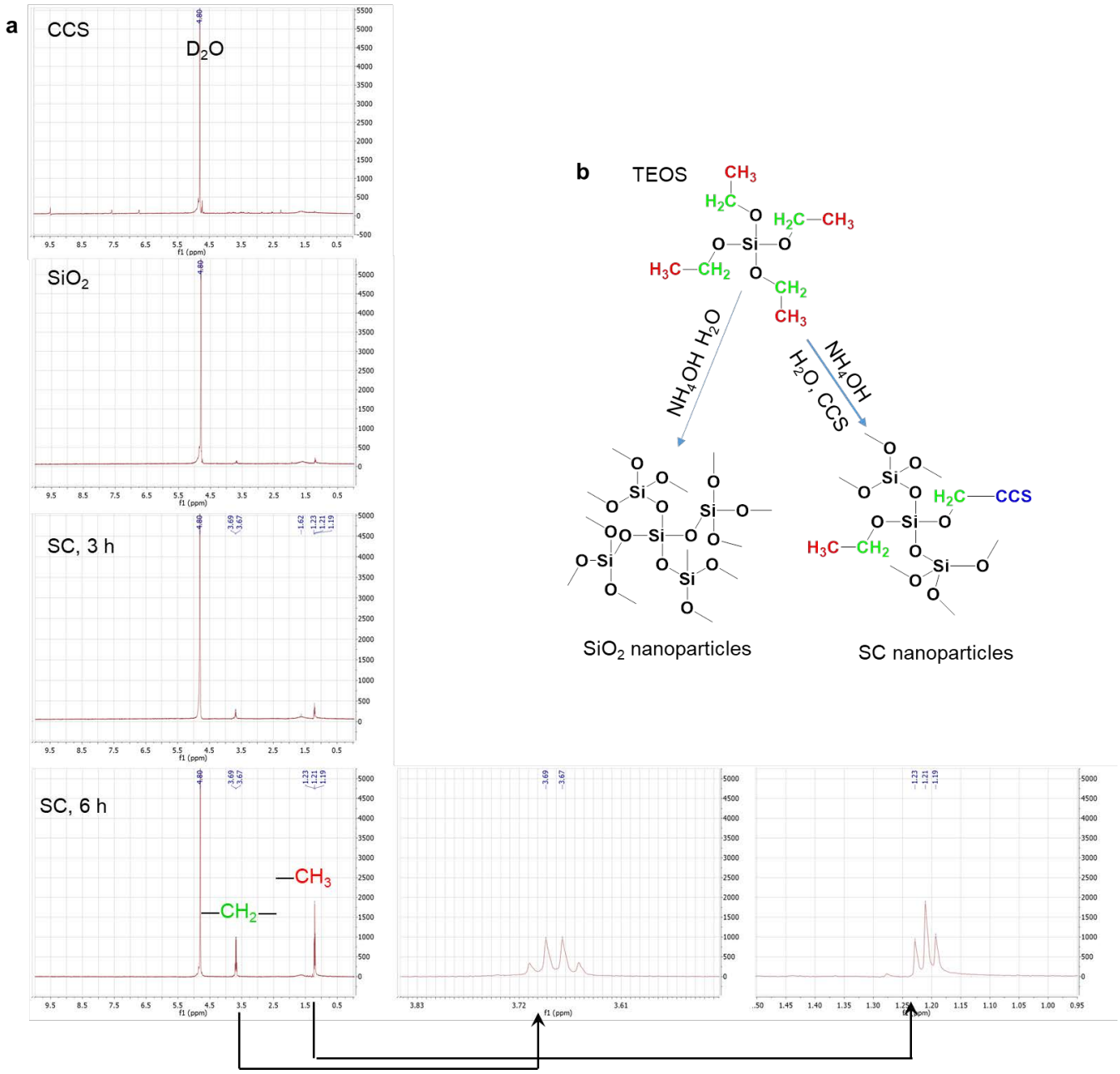

Supplementary Figure 5. ^{1}H NMR analysis of SC nanoparticles. (**a**), NMR spectra of CCS, SiO_2, and SC (made with 3 and 6 h of reaction) nanoparticles. Peaks for the methyl (around 1.2 ppm) and methylene (around 3.7 ppm) groups show up in the spectra of SC nanoparticles. (**b**), Taken together with the FTIR data shown in Supplementary Figure 4, we propose that the tetraethyl orthosilicate (TEOS) may react with CCS and leave some methyl and methylene groups in the resultant SC nanoparticles. D_2O is deuterium oxide that was used as the internal reference.

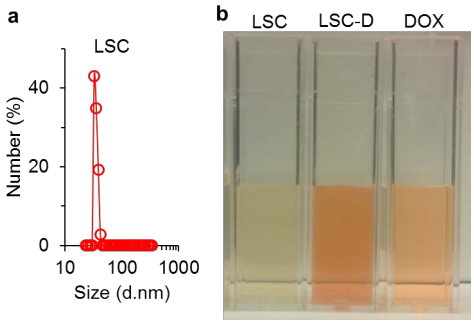

Supplementary Figure 6. Characterizations of LSC nanoparticles. (**a**), Size distribution of the LSC nanoparticles determined by dynamic light scattering (DLS). (**b**), Photograph of solutions of LSC nanoparticles, DOX-laden LSC (LSC-D) nanoparticles, and free DOX showing the excellent dispersibility of the LSC and LSC-D nanoparticles in deionized water.

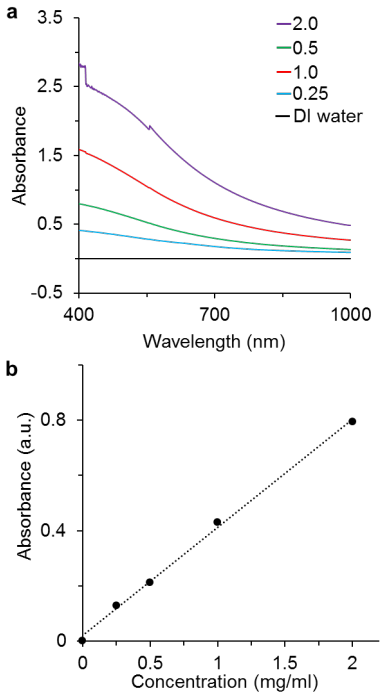

Supplementary Figure 7. UV-Vis analysis of LSC nanoparticles. (**a**), Ultraviolet-visible (UV-Vis) absorbance of deionized (DI) water and LSC nanoparticles of different concentrations (0.25-2.0 mg ml^{-1}) in DI water. (**b**), A linear correlation between concentration and the absorbance at 800 nm (for near infrared) is observable for the LSC nanoparticles.

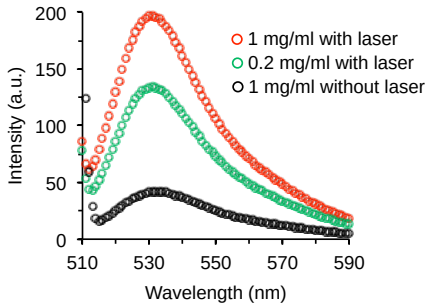

Supplementary Figure 8. Photodynamic effect of LSC nanoparticles. This is examined by the production of singlet oxygen by the nanoparticles dissolved in PBS under NIR laser irradiation. The production of singlet oxygen by the LSC nanoparticles without NIR irradiation is minimal. With NIR laser irradiation, the production of singlet oxygen by the LSC nanoparticles is concentration dependent. The NIR laser irradiation was at 1 W cm^{-2} for 1 min.

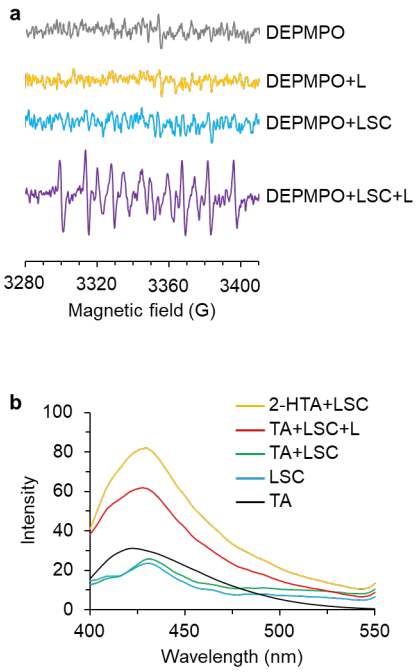

Supplementary Figure 9. Detection of hydroxyl radicals produced by LSC nanoparticles with laser irradiation. (**a**), Electron paramagnetic resonance spectra of the spin trap 5-(diethoxyphosphoryl)-5-methyl-1-pyrroline-N-oxide (DEPMPO) alone, DEPMPO with laser irradiation (DEPMPO+L), and DEPMPO mixed with LSC nanoparticles without or with NIR laser irradiation (DEPMPO+LSC or DEPMPO+LSC+L). Clear signals can be detected for the DEPMPO+LSC+L group, suggesting the hydroxyl (·OH) free radicals can be produced by the LSC nanoparticles with laser irradiation and trapped by DEPMPO. The LSC nanoparticles of 2 mg ml^{-1} were dissolved in DI water together with 20 mM DEPMPO for measurement. The laser irradiation was at 1 W cm^{-2} for 1 min. All the spectra are recorded and averaged from a total of 16 scans. (**b**), Fluorescence spectra of terephthalic acid (TA), LSC nanoparticles, TA mixed with LSC nanoparticles without or with NIR laser irradiation (TA+LSC or TA+LSC+L), and 2-Hydroxyterephthalic acid (2-HTA) mixed with LSC nanoparticles (2-HTA+LSC). The results show hydroxyl radicals (·OH) can be produced by LSC+L and reacted with TA to generate 2-HTA with stronger fluorescence. TA and 2-HTA of 82.1 nM were used in this measurement. The concentration of LSC nanoparticles was 2 mg ml^{-1}. The NIR laser irradiation was at 1 W cm^{-2} for 1 min.

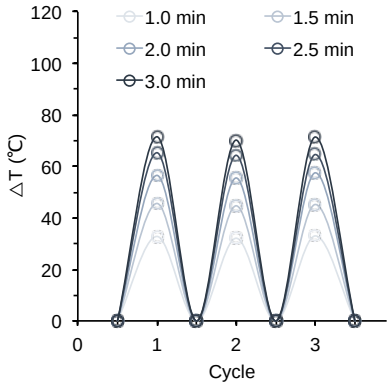

Supplementary Figure 10. Photothermal effect of LSC nanoparticles. The LSC nanoparticles (1 mg ml^{-1} in deionized water) were irradiated with different times (1.0-3.0 min) for three cycles. The change in temperature increases with the increase of irradiation time. After irradiated with a given time, the solutions of the LSC nanoparticles were passively cooled to room temperature before irradiated again. The photothermal effect of the LSC nanoparticles is similar among the three cycles. The NIR laser irradiation was at 1 W cm^{-2}.

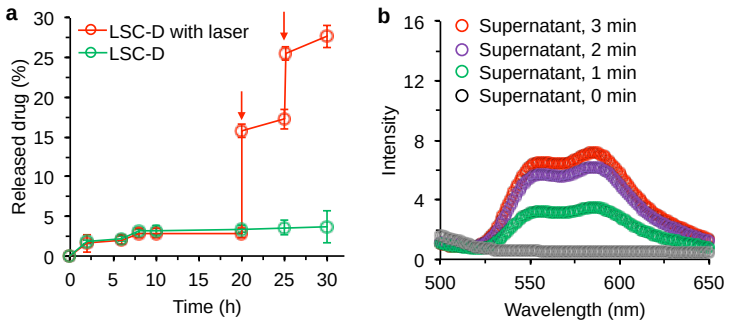

Supplementary Figure 11. NIR laser irradiation controlled drug release from LSC-D nanoparticles. (**a**), DOX release from the LSC-D nanoparticles in PBS can be precisely controlled with NIR laser irradiation. The arrows indicate laser irradiation at two different times. The NIR laser irradiation was at 1 W cm^{-2} for 1 min. Error bars represent s.d. (n = 3). (**b**), Fluorescence intensity of supernatant of LSC-D nanoparticle solution with the same DOX concentration after laser irradiation (1 W cm^{-2}) for 0, 1, 2, and 3 min, further showing the drug release can be precisely controlled by dosing the NIR irradiation.

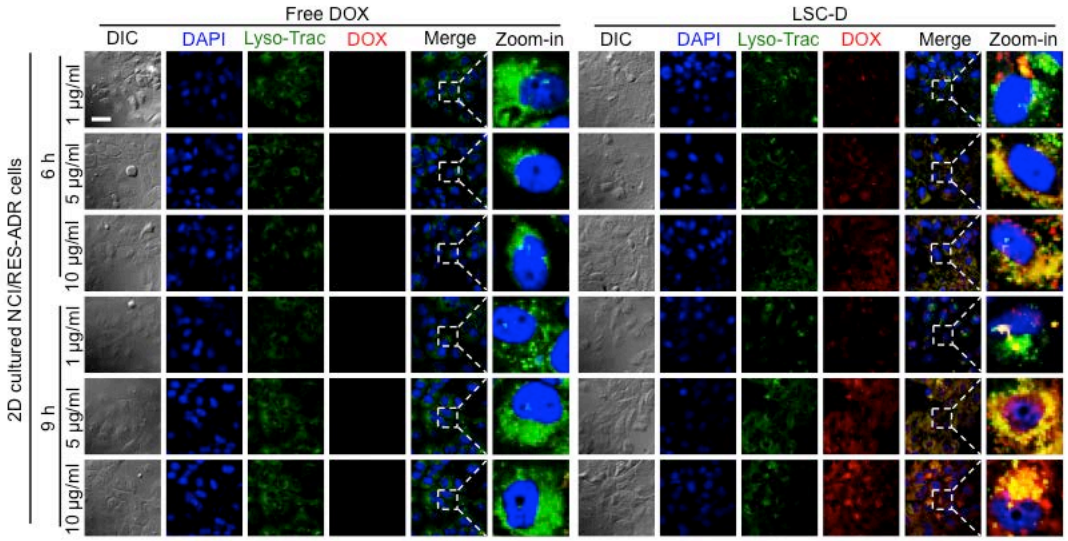

Supplementary Figure 12. NCI/RES-ADR cell uptake of free DOX versus LSC-D nanoparticles. The cells were incubated with different concentrations of free or encapsulated DOX for 6 or 9 h. The confocal fluorescence images show the NCI/RES-ADR cells can exclude free DOX but they do take up the LSC-D nanoparticles. However, the DOX is mainly located in the cytosol rather than nuclei in the cells with LSC-D treatment. DIC: differential interference contrast, and scale bar: 20 μm.

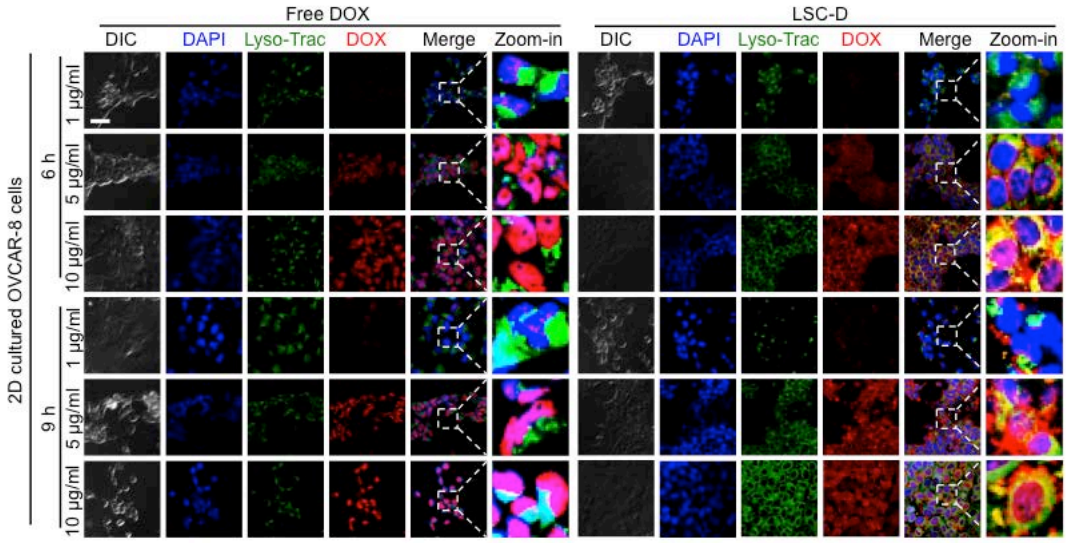

Supplementary Figure 13. OVCAR-8 cell uptake of free DOX versus LSC-D nanoparticles. The cells were incubated with different concentrations of free or encapsulated DOX for 6 or 9 h. The confocal fluorescence images show free DOX can enter and is located in the nuclei of the cells. For LSC-D treatment, DOX mainly stays in the cytosol although some also enters the cell nuclei dependent on the incubation time and DOX concentration. DIC: differential interference contrast, and scale bar: 20 μm.

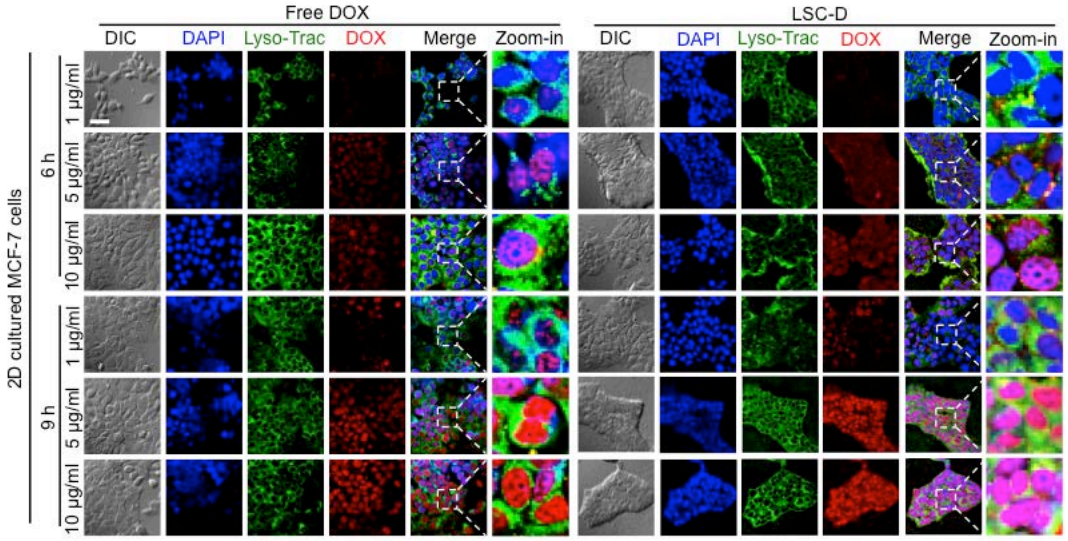

Supplementary Figure 14. MCF-7 cell uptake of free DOX versus LSC-D nanoparticles. The cells were incubated with different concentrations of free or encapsulated DOX for 6 or 9 h. The confocal fluorescence images show free DOX can enter and is located in the nuclei of the cells. For LSC-D treatment, DOX mainly stays in the cytosol although some also enters the cell nuclei dependent on the incubation time and DOX concentration. DIC: differential interference contrast, and scale bar: 20 μm.

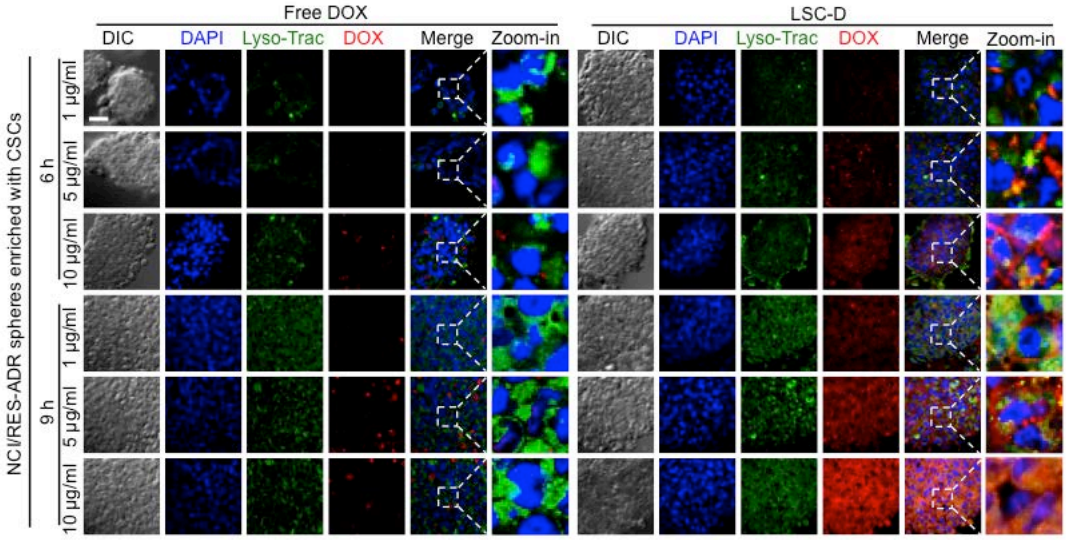

Supplementary Figure 15. Uptake of free DOX versus LSC-D nanoparticles by NCI/RES-ADR sphere cells. The cells were incubated with different concentrations of free or encapsulated DOX for 6 or 9 h. The confocal fluorescence images show the NCI/RES-ADR sphere cells can exclude free DOX but they do take up the LSC-D nanoparticles. However, the DOX is mainly located in the cytosol rather than nuclei in the cells with LSC-D treatment. DIC: differential interference contrast, and scale bar: 40 μm.

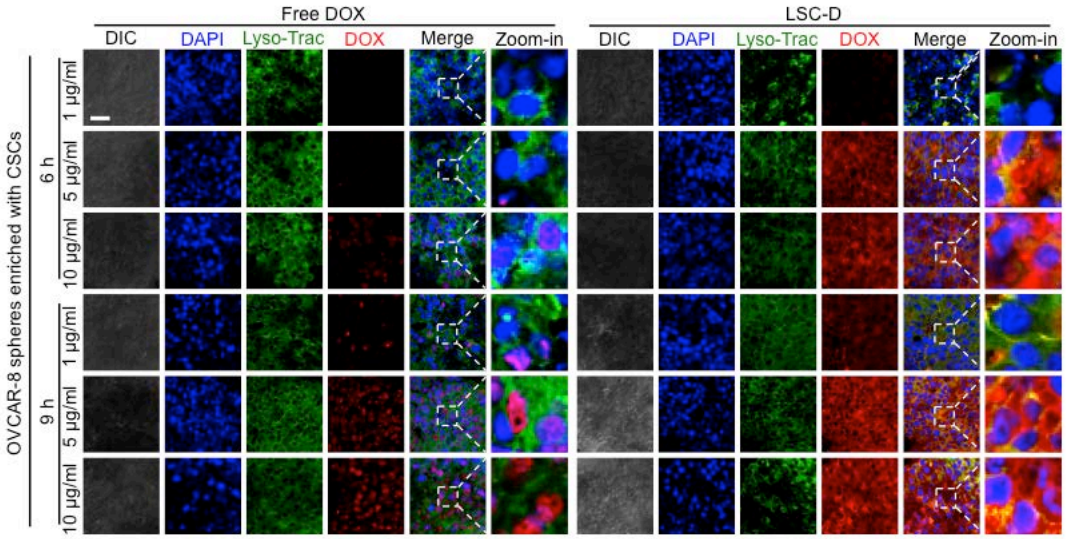

Supplementary Figure 16. Uptake of free DOX versus LSC-D nanoparticles by OVCAR-8 sphere cells. The cells were incubated with different concentrations of free or encapsulated DOX for 6 or 9 h. The confocal fluorescence images show free DOX can enter and is located in the nuclei of the cells, but the fluorescence intensity of DOX is weaker than that in the 2D cultured OVCAR-8 cells under the same treatment conditions. The cells also take up the LSC-D nanoparticles although the DOX is mainly in the cytosol of the sphere cells with the LSC-D treatment. DIC: differential interference contrast, and scale bar: 40 μm.

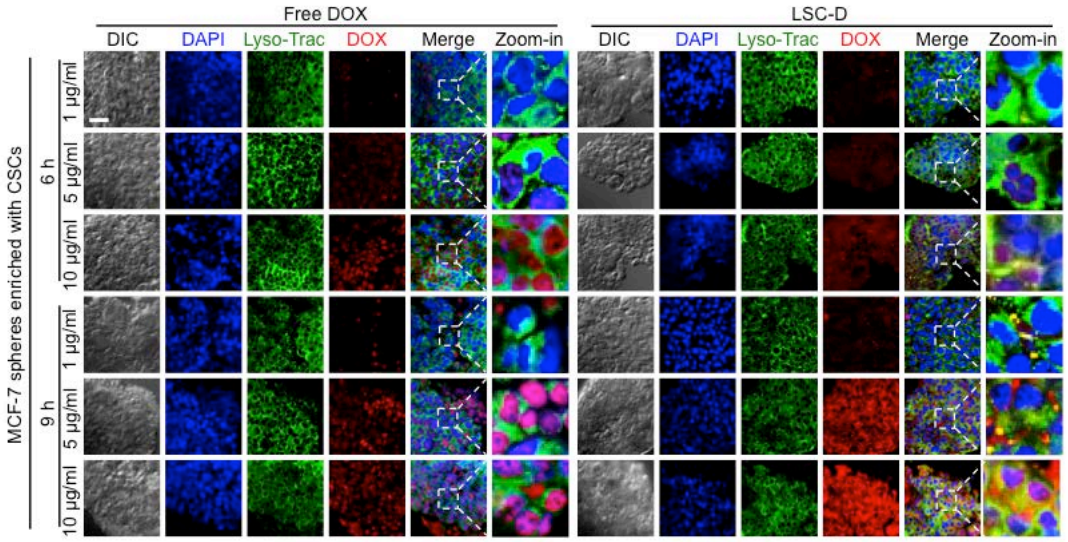

Supplementary Figure 17. Uptake of free DOX versus LSC-D nanoparticles by MCF-7 sphere cells. The cells were incubated with different concentrations of free or encapsulated DOX for 6 or 9 h. The confocal fluorescence images show free DOX can enter and is located in the nuclei of the cells, but the fluorescence intensity of DOX is weaker than that in the 2D cultured OVCAR-8 cells under the same treatment conditions. The cells also take up the LSC-D nanoparticles although the DOX is mainly located in the cytosol of the sphere cells with LSC-D treatment. DIC: differential interference contrast, and scale bar: 40 μm.

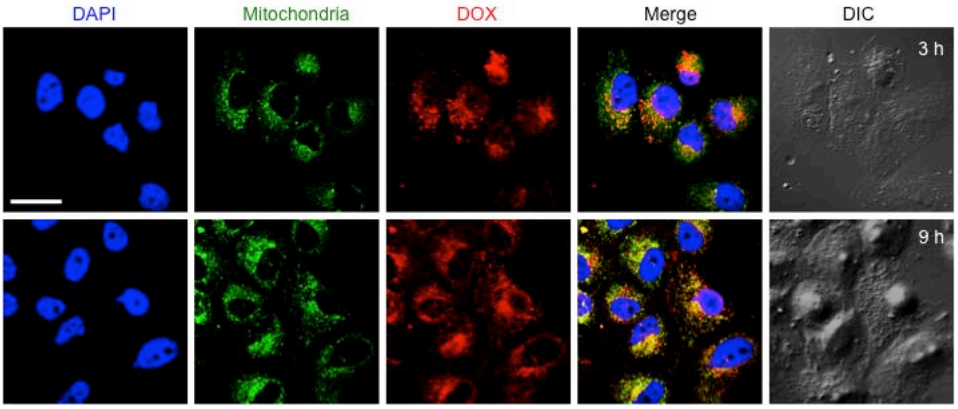

Supplementary Figure 18. Mitochondria targeting with LSC-D nanoparticles. Confocal images of NCI/RES-ADR cells treated with LSC-D nanoparticles for 3 or 9 h and then stained for mitochondria, showing the mitochondria targeting capability of the nanoparticles. Scale bar: 20 μm.

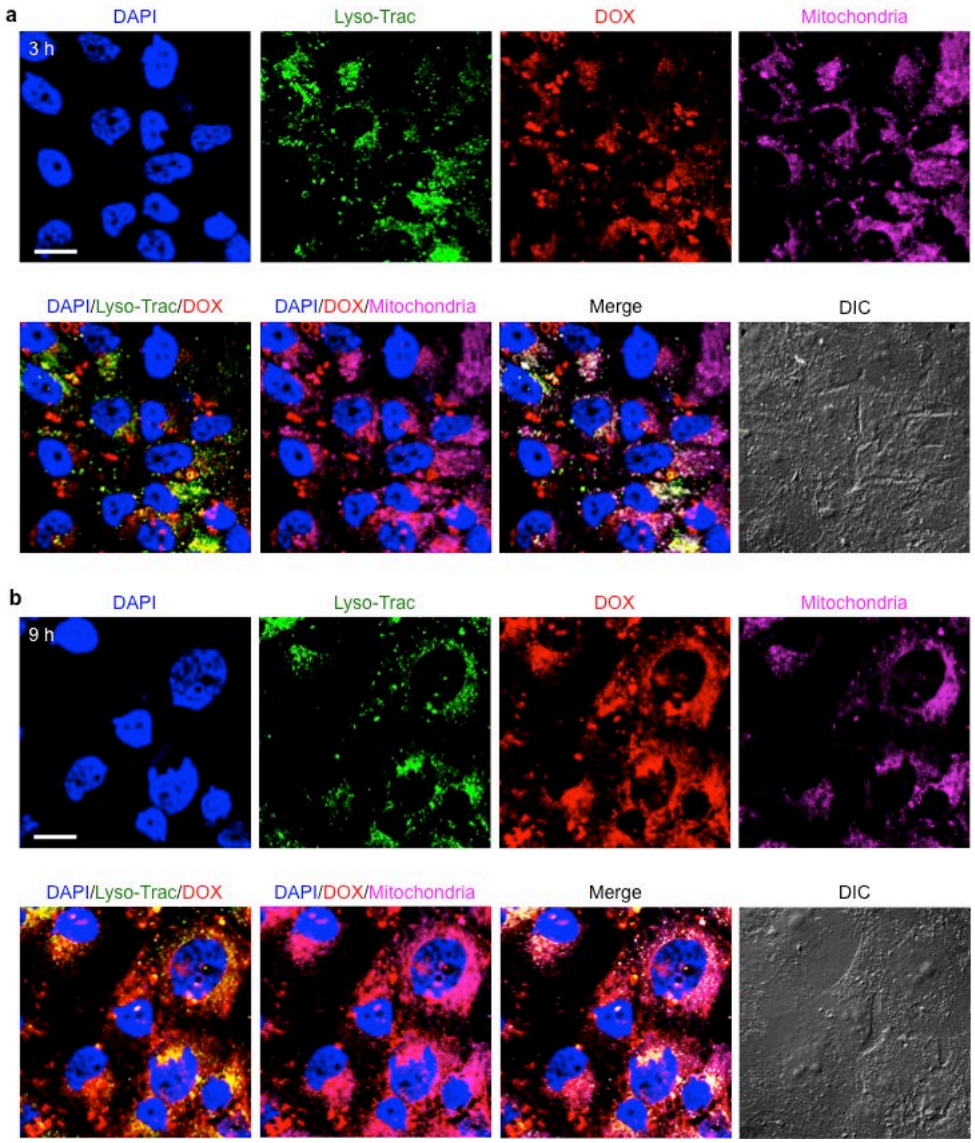

Supplementary Figure 19. Intracellular distribution of LSC-D nanoparticles. Confocal images of NCI/RES-ADR cells treated with LSC-D nanoparticles for (**a**), 3 h, and (**b**), 9 h, and then stained for both endo/lysosome and mitochondria, showing part of the LSC-D nanoparticles are co-localized with endo/lysosome and part of them are co-localized with mitochondria. The results suggest that the cells take up the LSC-D nanoparticles via endocytosis and can target the mitochondria. Scale bars: 20 μm.

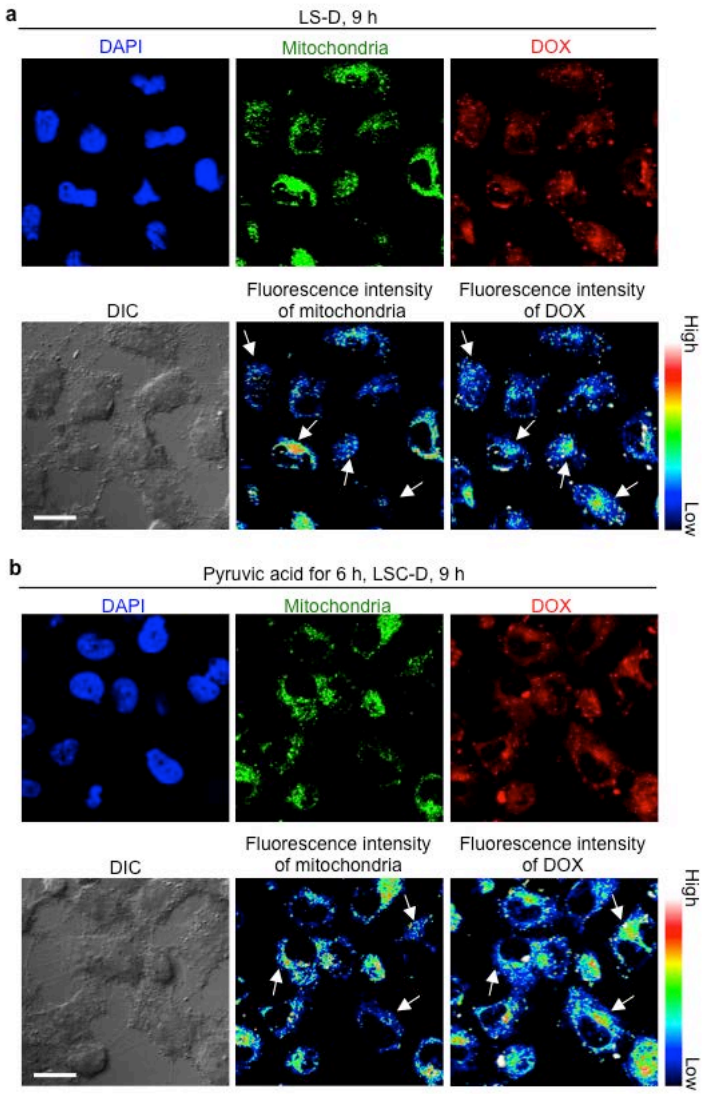

Supplementary Figure 20. Confocal fluorescence microscopy study showing minimal mitochondria targeting with lipid coated silica nanoparticles or with pre-blocking using pyruvic acid. (**a**), Confocal images of NCI/RES-ADR cancer cells treated with DOX-laden lipid coated silica (LS-D) nanoparticles (with no carbon sphere or pyruvate) for 9 h, and then stained for mitochondria. The data show the distribution of LS-D nanoparticles is different from that of mitochondria. Arrows indicate that some of the cells in which the distribution of LS-D nanoparticles and mitochondria is evidently different. (**b**), Confocal images of NCI/RES-ADR cancer cells pre-blocked with pyruvic acid (5 μl ml^{-1}) for 6 h, and then treated with DOX-laden LSC (LSC-D) nanoparticles together with pyruvic acid for another 9 h, showing the distribution of LSC-D nanoparticles is evidently different from mitochondria. The data indicate pre-blocking with pyruvic acid minimizes mitochondria targeting by the LSC-D nanoparticles and the crucial role of the pyruvate group on the LSC-D nanoparticles for mitochondria targeting. Arrows indicate that some of the cells in which the distribution of LSC-D nanoparticles and mitochondria is evidently different. Scale bars: 20 μm.

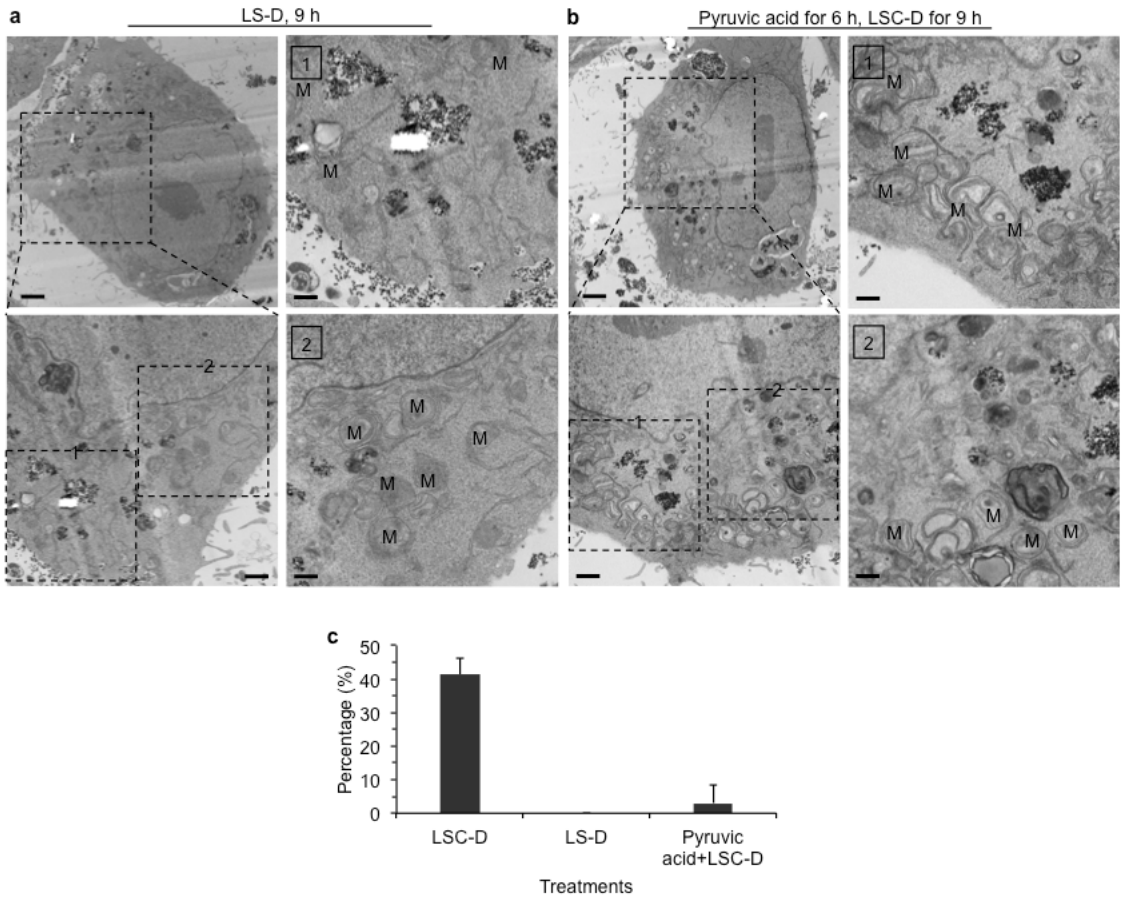

Supplementary Figure 21. Transmission electron microscopy study showing minimal mitochondria targeting with lipid coated silica nanoparticles or with pre-blocking using pyruvic acid. (**a**), Representative transmission electron microscopy (TEM) images of NCI/RES-ADR cells treated with LS-D nanoparticles for 9 h, showing the LS-D cannot target mitochondria. M: mitochondria. Scare bar: 2, 1, and 0.5 μm in top left, bottom left, and right images, respectively. (**b**), Representative TEM images of NCI/RES-ADR cells pre-blocked with pyruvic acid (5 μl ml^{-1}) for 6 h, and then treated with LSC-D nanoparticles together with pyruvic acid for another 9 h, showing minimized distribution of LSC-D nanoparticles in mitochondria. Scare bar: 2, 1, and 0.5 μm in top left, bottom left, and right images, respectively. (**c**), Quantitative data on the percentage of LSC-D and LS-D nanoparticles in mitochondria in the cancer cells. Of note, only nanoparticles that escaped the endo/lysosomes in the cancer cells were counted for the quantification. The data show the LSC nanoparticles could not target mitochondria. In contrast, the LSC-D nanoparticles could target the mitochondria, which can be blocked with pyruvic acid. Error bars represent s.d. (n = 5).

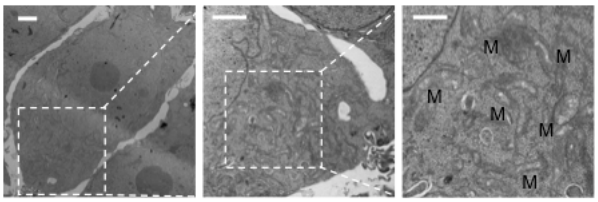

Supplementary Figure 22. Representative TEM images of NCI/RES-ADR cancer cells incubated with free DOX for 9 h. The cellular structure is similar to that of the cells treated with saline (Figure 3b), which is probably due to the drug resistant property of the cells and little DOX could enter the cells. The concentration of DOX was 10 μg ml^{-1}. M indicates mitochondrion. Scare bar: 2, 2, and 1 μm for the left, middle, and right images, respectively.

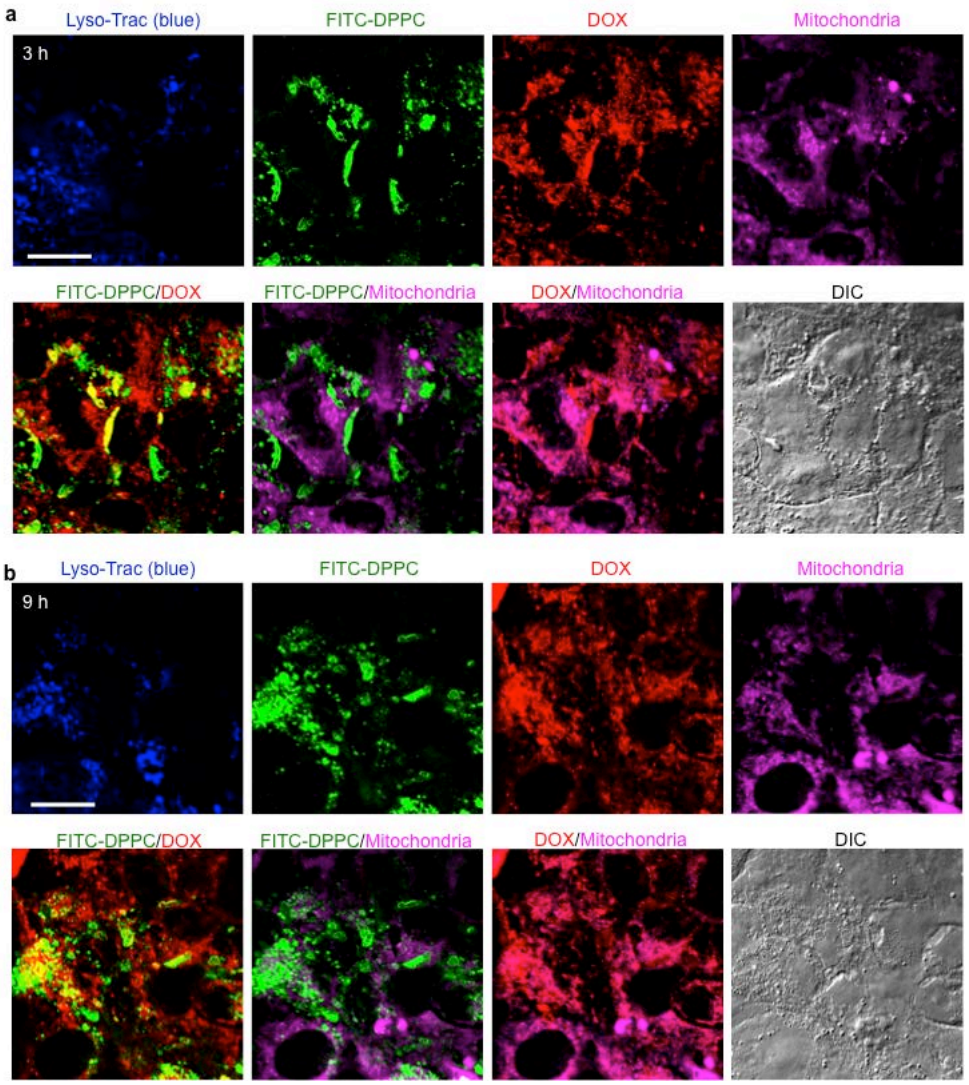

Supplementary Figure 23. Intracellular distribution of DPPC membrane and nanoparticles. The fluorescein isothiocyanate (FITC) labeled DPPC (FITC-DPPC) was used to form the membrane coating on the LSC nanoparticles. Confocal images of NCI/RES-ADR cells treated with LSC-D nanoparticles for (**a**), 3 h, and (**b**), 9 h, and then stained for mitochondria, showing most of the nanoparticles (indicated by the red fluorescence of DOX) are co-localized with mitochondria but not FITC-DPPC membrane. Scare bars: 20 μm.

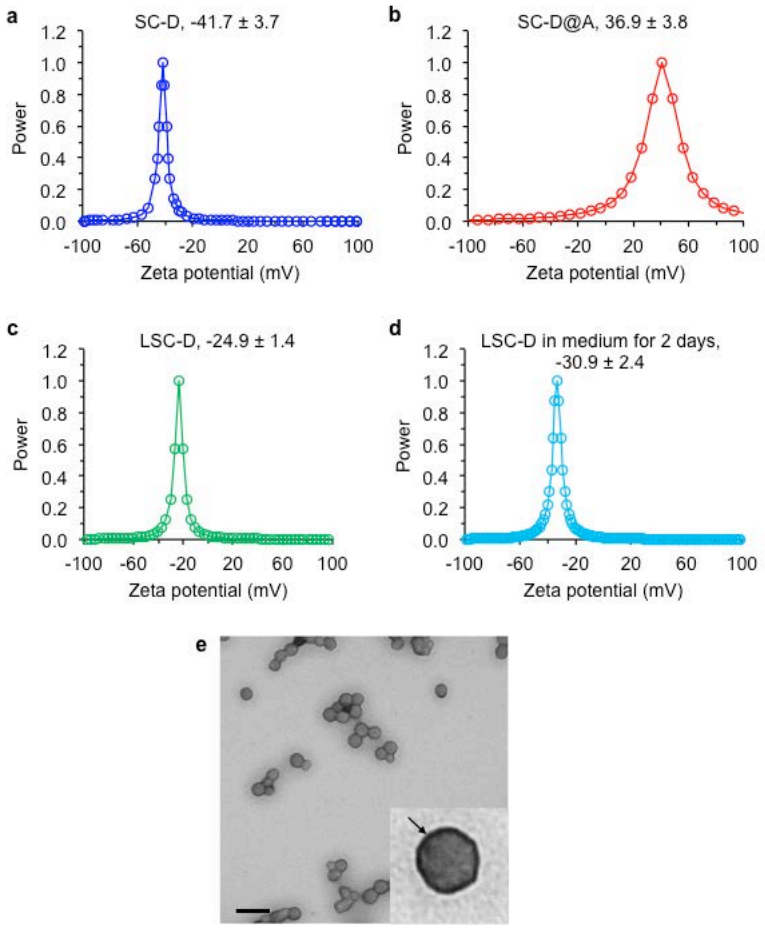

Supplementary Figure 24. Stability of LSC-D nanoparticles *in vitro*. (**a-c**), Zeta potential of SC-D nanoparticles, APTMS modified SC-D nanoparticles (SC-D@A), and LSC-D nanoparticles. The zeta potential indicates successful modification of APTEM on the nanoparticles (positive) and successful coating of lipid membrane on the nanoparticles (negative, similar to the zeta potential of liposomes). (**d-e**), LSC-D nanoparticles are dispersed in medium (with 10% fetal bovine serum) for 2 days, and then collected and re-suspended in DI water. Both the zeta potential data (d) and TEM image (e) indicate that the membrane coated on LSC-D nanoparticles is stable in medium. Arrow indicates the lipid membrane on the surface of LSC-D nanoparticles. Scare bar: 100 nm.

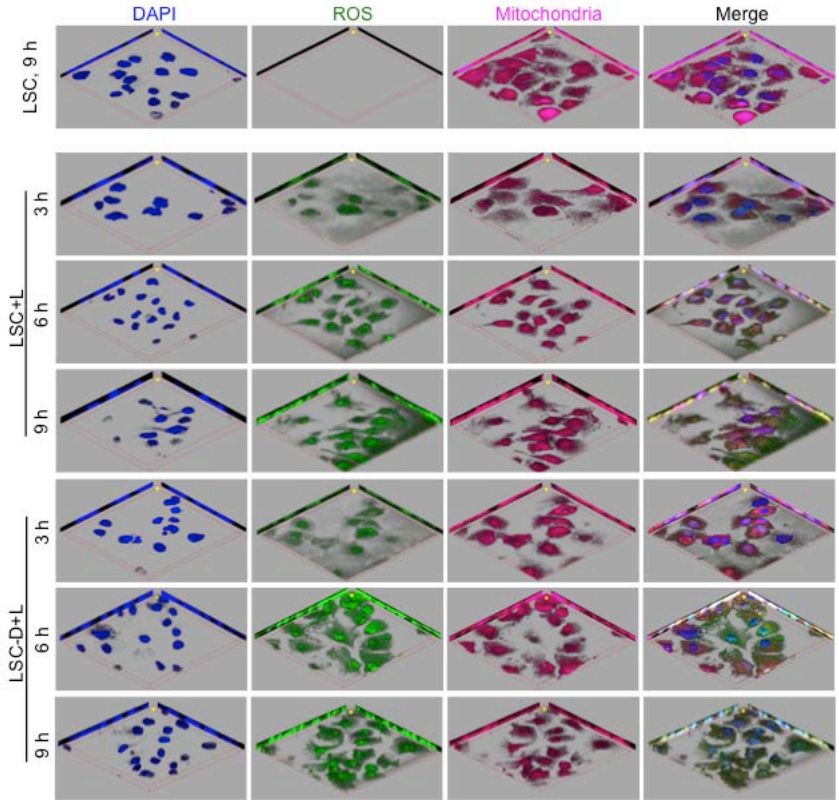

Supplementary Figure 25. Confocal images showing ROS distribution in cells in 3D. The fluorescence of reactive oxygen species (ROS) is co-localized with mitochondria in the cells treated with LSC/LSC-D nanoparticles and laser irradiation (L). The NIR laser irradiation was at 1 W cm^{-2} for 1 min.

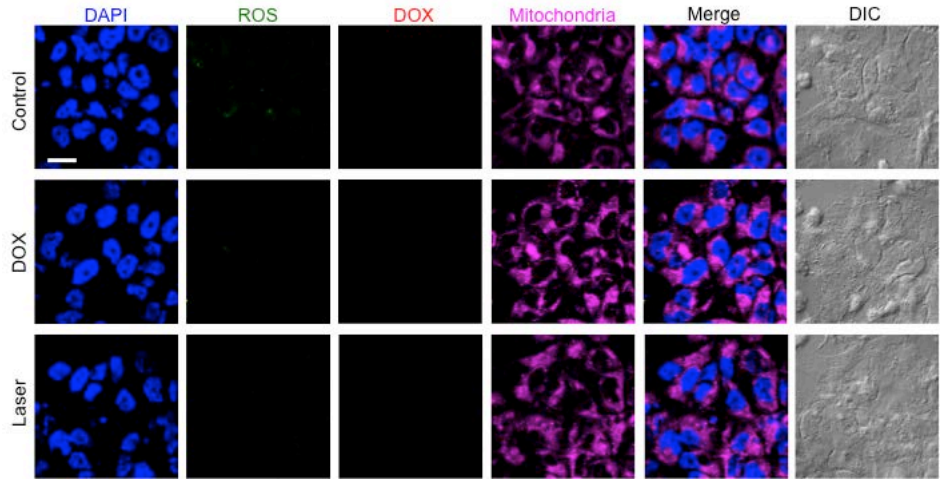

Supplementary Figure 26. ROS detection in cells treated with free DOX or NIR laser irradiation. The results indicate that minimal ROS could be generated in the NCI/RES-ADR cells after treated with free DOX for 9 h or irradiated with NIR laser at 1 W cm^{-2} for 1 min. The concentration of DOX was 10 μg ml^{-1}. Scare bar: 20 μm.

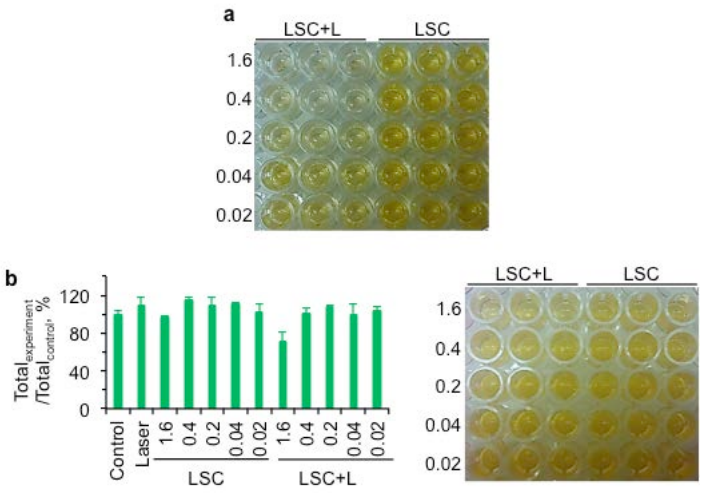

Supplementary Figure 27. NADH and NDA^+ measurement in NCI/RES-ADR cells. (**a**), Photograph of the NADH assay in NCI/RES-ADR cells treated with LSC nanoparticles with or without laser irradiation. The corresponding quantitative data are shown in Fig. 3d. (**b**), Data on the total amount of NADH & NDA^+ showing no significant difference between cells with and without laser irradiation. This suggests the ROS decreases the amount NADH by converting/oxidizing it into NAD^+ so that the sum of NDA^+ & NADH does not change in cells. The NIR laser irradiation was at 1 W cm^{-2} for 1 min. Error bars represent s.d. (n = 3). Control cells were cultured in medium without any treatment.

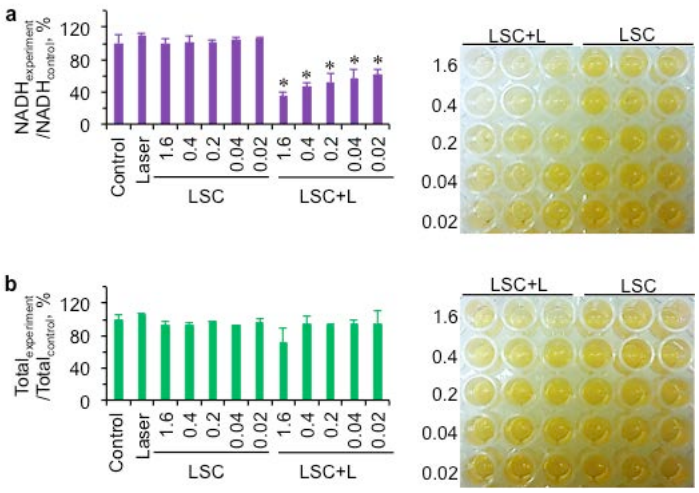

Supplementary Figure 28. NADH and NDA$^+$ measurement in OVCAR-8 cells. (**a**), Measurement of NADH in OVCAR-8 cells treated with LSC nanoparticles with or without laser irradiation, showing the LSC nanoparticles can significantly reduce the amount of NADH in cells after NIR laser irradiation. Error bars represent s.d. (n = 3). The LSC+L group is compared with the LSC group with the same LSC concentration, as well as the PBS and PBS+L groups. *p < 0.05 (Kruskal-Wallis H-test). (**b**), Total NADH & NDA$^+$ measurement, showing no significant difference between cells with and without laser irradiation. This suggests the ROS decreases the amount NADH by converting/oxidizing it into NAD$^+$. The NIR laser irradiation was at 1 W cm^{-2} for 1 min. Error bars represent s.d. (n = 3). Control cells were cultured in medium without any treatment.

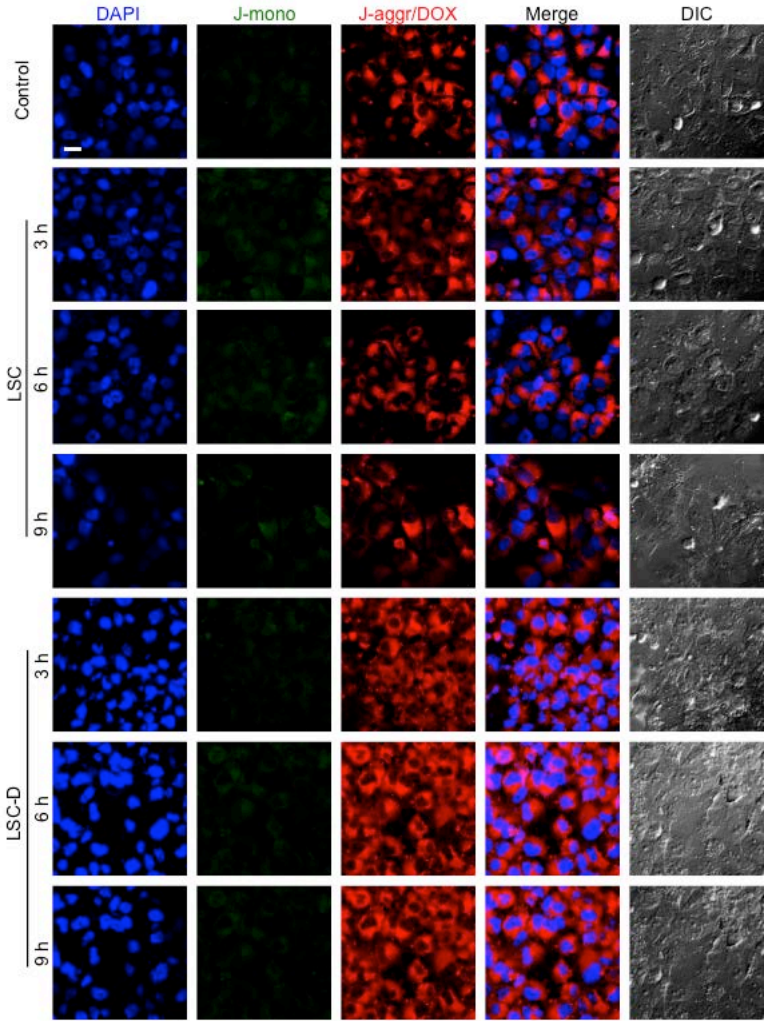

Supplementary Figure 29. Mitochondrial membrane potential in NCI/RES-ADR cells treated with nanoparticles without NIR irradiation. The cells were treated with LSC or LSC-D nanoparticles for 12 h, and stained with JC-1 (a Mitochondrial membrane potential dye) at 3, 6, and 9 h after the treatment. Control cells were cultured in medium without any nanoparticles. The data show high mitochondrial membrane potential (strong red fluorescence with minimal green staining) in the cells. For the cells treated with LSC-D nanoparticles, both the JC-1 stain and DOX contribute to the red fluorescence. Scare bar: 20 μm.

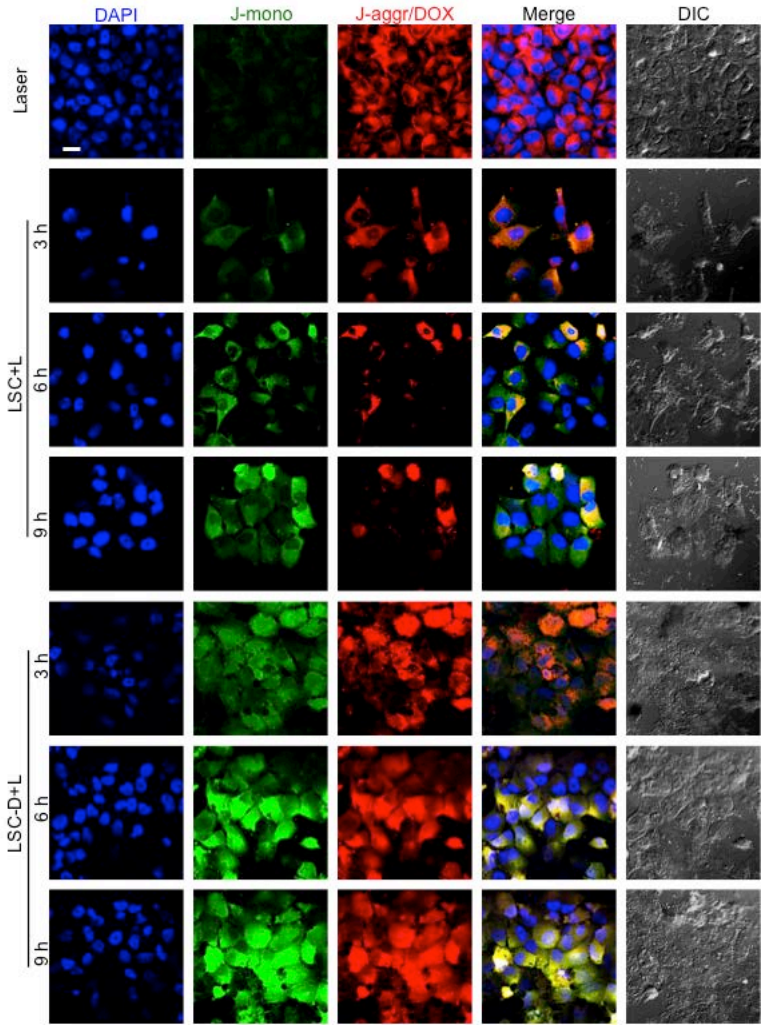

Supplementary Figure 30. Mitochondrial membrane potential in NCI/RES-ADR cells treated with nanoparticles and NIR irradiation. The cells were treated with LSC or LSC-D nanoparticles for 12 h, irradiated with NIR laser, and stained with JC-1 (a Mitochondrial membrane potential dye) at 3, 6, and 9 h after the treatment. The data show low mitochondrial membrane potential (strong green fluorescence) in the cells, suggesting the dysfunction of mitochondria. For the cells treated with LSC-D nanoparticles, both the JC-1 stain and DOX contribute to the red fluorescence. The NIR laser irradiation was at 1 W cm^{-2} for 1 min. The laser irradiation alone has minimal impact on the mitochondrial membrane potential in NCI/RES-ADR cells. Scare bar: 20 μm.

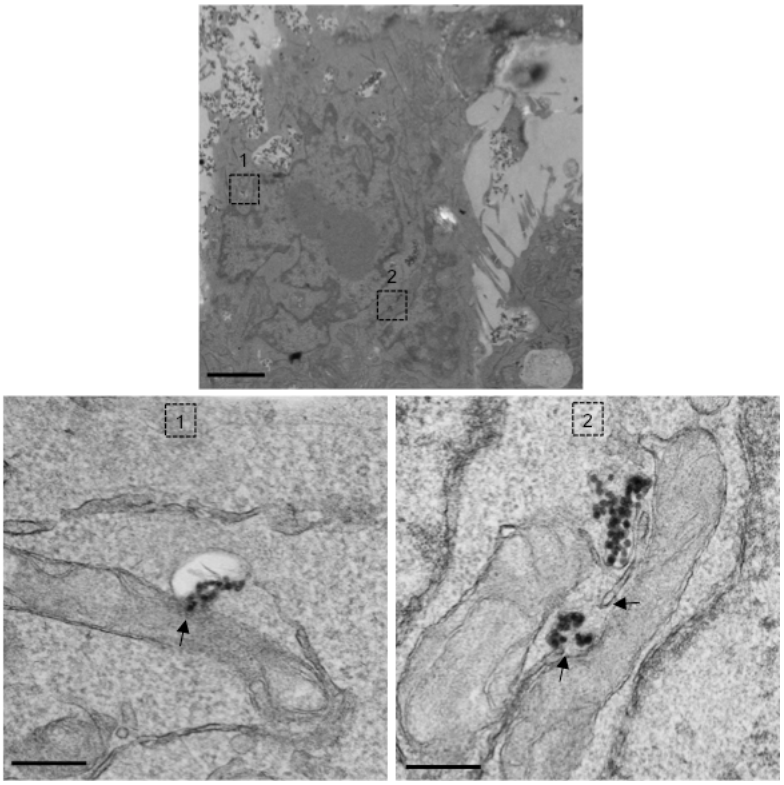

Supplementary Figure 31. Damage to mitochondrial membrane in NCI/RES-ADR cells treated with nanoparticles and NIR irradiation. Representative TEM images of NCI/RES-ADR cells incubated with LSC-D nanoparticles for 9 h and irradiated with NIR laser for 1 min at1 W cm^{-2}. The membrane of mitochondria is not integral at the locations (arrows) with LSC-D nanoparticles after laser irradiation. Scare bar: 2 and 0.2 μm for top and bottom images, respectively.

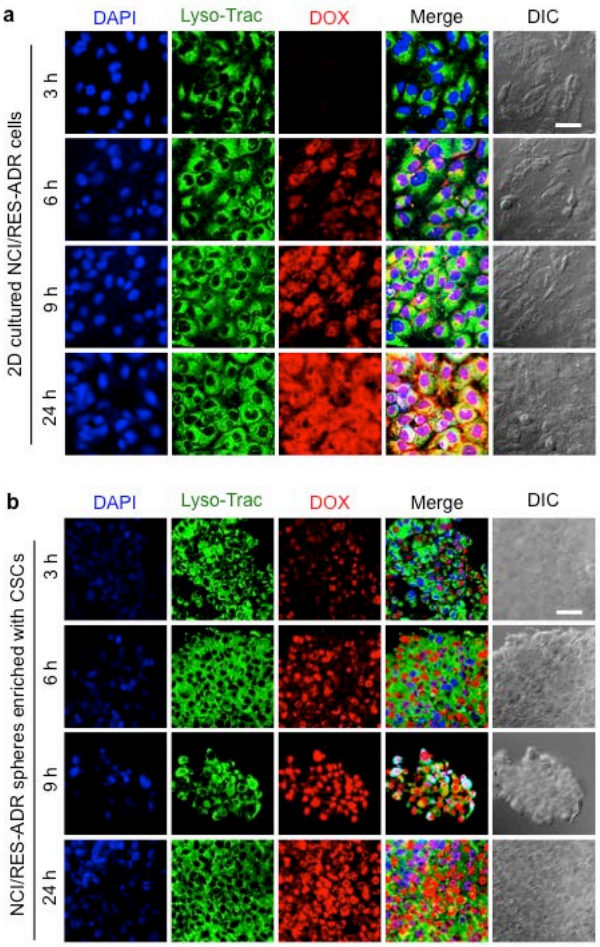

Supplementary Figure 32. Overcoming drug resistance by targeted production of reactive oxygen species in mitochondria. Confocal and differential interference contrast (DIC) images of (**a**), 2D cultured NCI/RES-ADR cells and (**b**), the NCI/RES-ADR spheres enriched with cancer stem-like cells (CSCs), showing the LSC+L treatment compromises their capability of drug resistance so that free DOX can enter the cells. The cells were incubated with LSC nanoparticles for 9 h and irradiated with NIR laser for 1 min at 1 W cm^{-2}. Then, the treated cells were incubated with free DOX (10 μg ml^{-1}) for 3-24 h. Scale bar: 20 and 40 μm in (a) and (b), respectively.

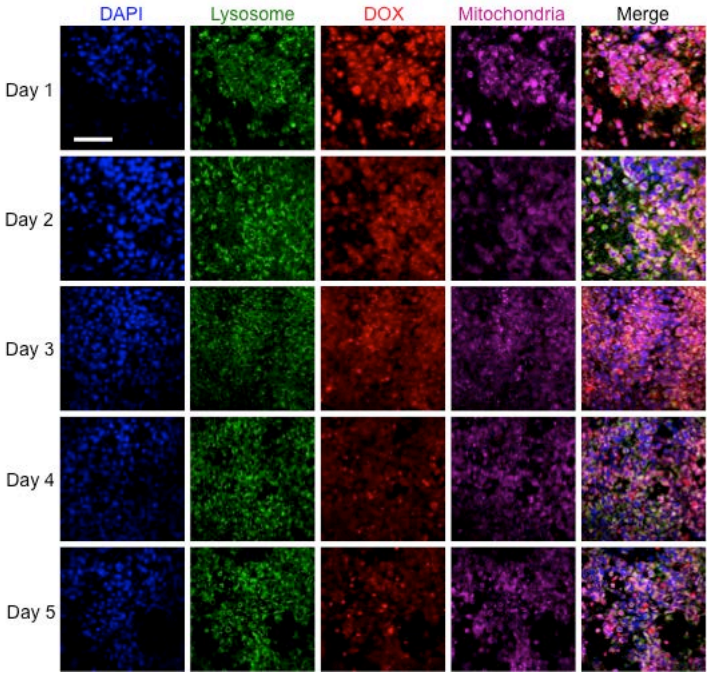

Supplementary Figure 33. Reducing drug resistance of multidrug resistant NCI/RES-ADR cells with LSC nanoparticles and laser irradiation. The NCI/RES-ADR cells were cultured with LSC nanoparticles for 3 h and then irradiated with laser (1 W cm^{-2} for 1 min, LSC+L). Afterward, the cells were cultured with free DOX for 3 h at 1-5 days after the laser irradiation. The data show the drug resistance of NCI/RES-ADR cells can be reduced for at least 5 days by the LCS+L treatment. Scale bar: 100 μm.

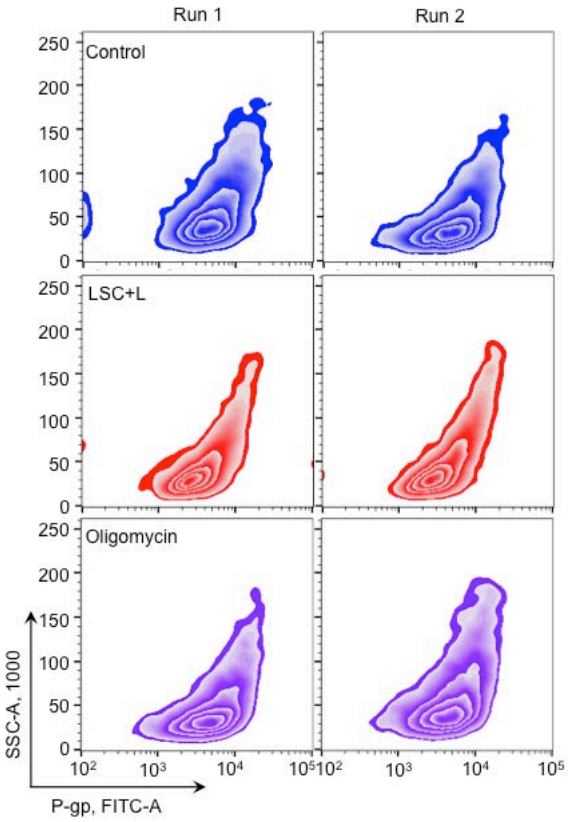

Supplementary Figure 34. Decreased expression of P-gp in NCI/RES-ADR cancer cells treated with LSC nanoparticles and NIR laser irradiation. Flow cytometry analysis of P-gp expression in cancer cells treated with saline, **LSC nanoparticles and NIR laser irradiation** (LSC+L), and oligomycin (12 h, 200 ng ml^{-1}). These are two independent runs in addition to that shown in Fig. 4b. The LSC+L treatment was conducted by incubating the cells with the LSC nanoparticles for 12 h, and then irradiated with NIR laser at 1 W cm^{-2} for 1 min. The cells were permeabilized for the flow cytometry analysis.

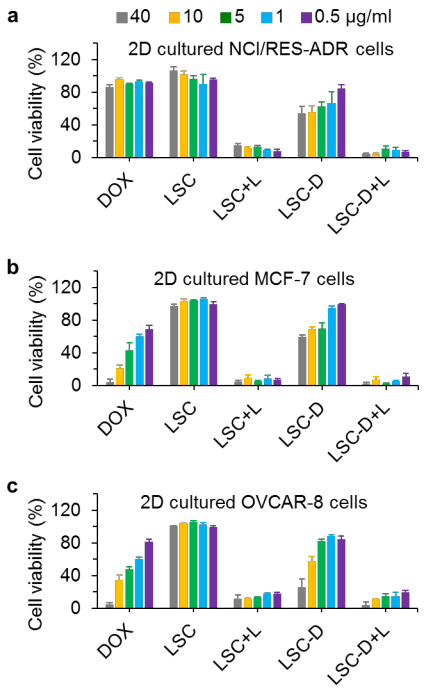

Supplementary Figure 35. Enhanced anticancer capacity of LSC-D nanoparticles under NIR laser irradiation *in vitro*. Viability of (**a**) NCI/RES-ADR, (**b**) MCF-7, and (**c**) OVCAR-8 cancer cells after treated with free DOX, LSC nanoparticles, and DOX-laden LSC (LSC-D) nanoparticles at different concentrations (0.5-40 μg ml^{-1}) without or with NIR laser (L) irradiation (at 1 W cm^{-2} for 1 min). Error bars represent s.d. (n = 3). The viability was measured using cell counting kit-8 (CCK-8) assay. Due to the decrease of NADH by ROS oxidization in the LSC+L treatment group and the reliance on NADH of the CCK-8 assay for measuring cell viability, the viability data for the LSC+L group are misleading.

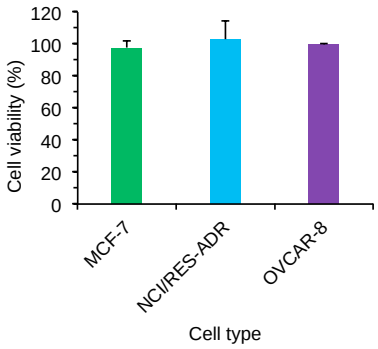

Supplementary Figure 36. Effect of NIR irradiation alone on cell viability. The data show that the laser irradiation (1 W cm^{-2} for 1 min) alone has minimal impact on the viability of MCF-7, NCI/RES-ADR, and OVCAR-8 cells. Error bars represent s.d. (n = 3).

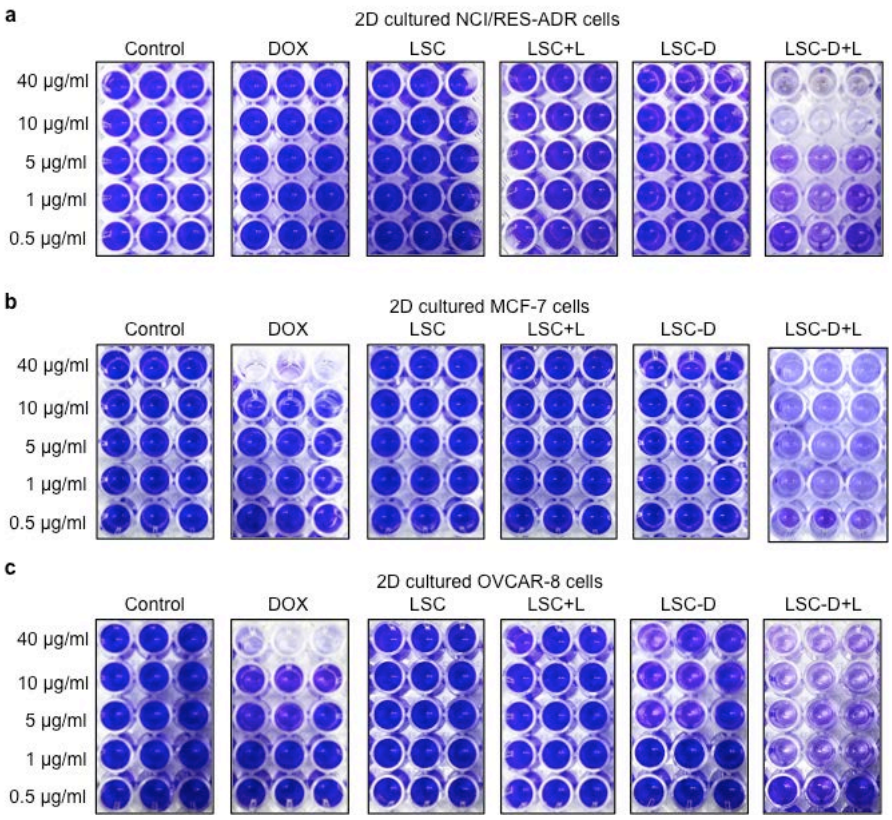

Supplementary Figure 37. Enhanced antitumor capacity of LSC-D nanoparticles under NIR laser irradiation *in vitro*. Photographs of crystal violet assay of (**a**), NCI/RES-ADR, (**b**), MCF-7, and (**c**), OVCAR-8 cancer cells after treated with free DOX, LSC nanoparticles, and DOX-laden LSC (LSC-D) nanoparticles at different concentrations (0.5-40 μg ml^{-1}) without or with NIR laser (L) irradiation (1 W cm^{-2} for 1 min). Control cells were cultured in medium without any treatment.

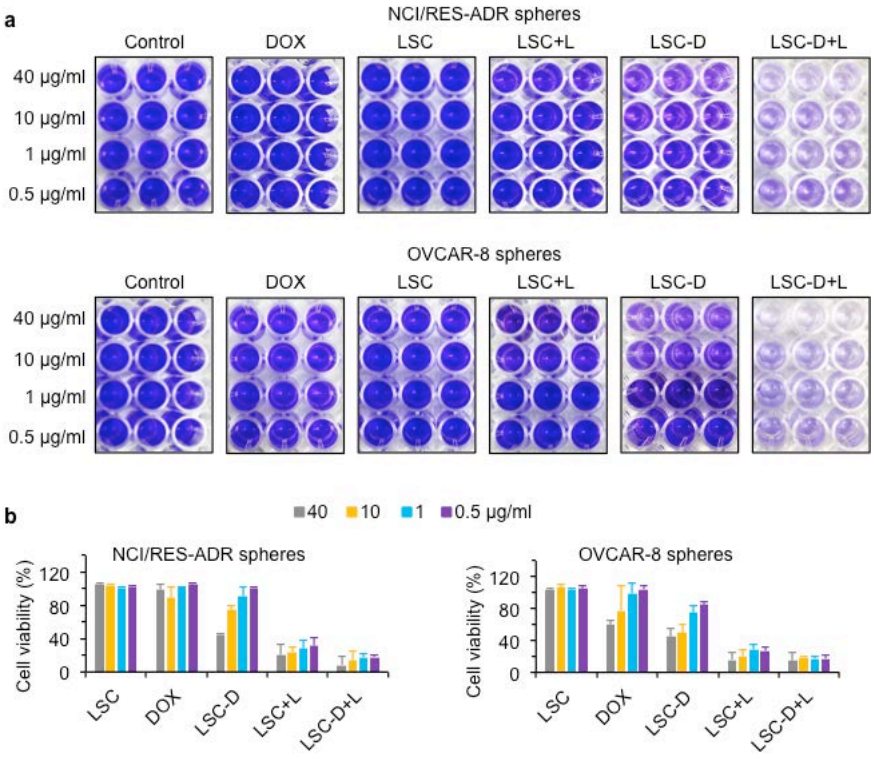

Supplementary Figure 38. Enhanced capacity of LSC-D nanoparticles to kill spheres enriched with cancer stem-like cells (CSCs) under NIR laser irradiation *in vitro*. (**a**), Photographs of crystal violet assay of CSC-enriched NCI/RES-ADR and OVCAR-8 spheres after treated with free DOX, LSC nanoparticles, and DOX-laden LSC (LSC-D) nanoparticles at different concentrations (0.5-40 μg ml^{-1}) without or with NIR laser (L) irradiation (1 W cm^{-2} for 1 min). Control cells were cultured in medium without any treatment. (**b**), Viability of CSC-enriched NCI/RES-ADR and OVCAR-8 spheres after treated with free DOX, LSC nanoparticles, and DOX-laden LSC (LSC-D) nanoparticles at different concentrations (0.5-40 μg ml^{-1}) without or with NIR laser (L) irradiation (1 W cm^{-2} for 1 min). Error bars represent s.d. (n = 3). The viability was determined by cell counting kit-8 (CCK-8) assay. Similar to 2D cells (Supplementary Fig. 29), the LSC+L groups are misleading due to the decrease of NADH by ROS oxidization in the LSC+L treatment group while the CCK-8 assay relies on NADH.

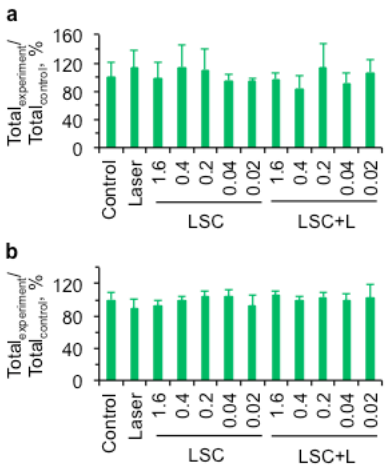

Supplementary Figure 39. Total NADH & NDA$^+$ in NCI/RES-ADR and OVCAR-8 spheres. (**a**), NCI/RES-ADR spheres. (**b**), OVCAR-8 spheres. The data show no difference between cells with and without laser irradiation in terms of the total NDA$^+$ & NADH. This suggests the ROS can only decrease the amount NADH by converting/oxidizing it into NAD$^+$. The NIR laser irradiation was at 1 W cm^{-2} for 1 min. Error bars represent s.d. (n = 3). Control cells were cultured in medium without any treatment.

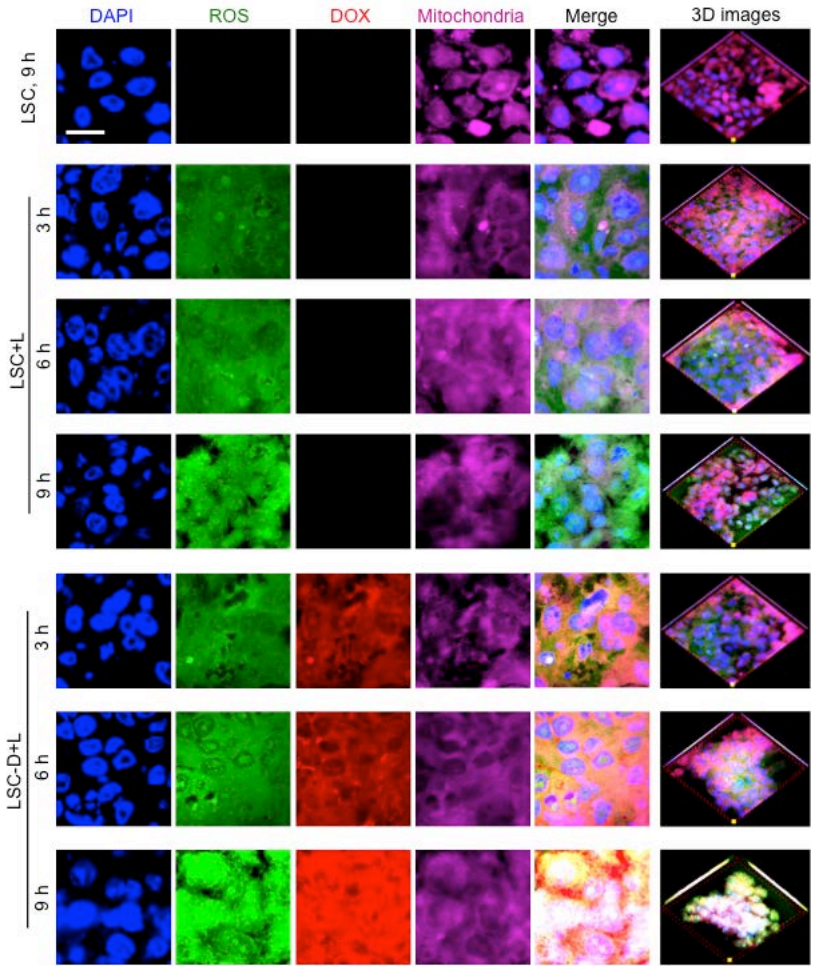

Supplementary Figure 40. Specific production of ROS in mitochondria of NCI/RES-ADR sphere cells. The NCI/RES-ADR spheres were incubated with LSC or LSC-D nanoparticles for 12 h, followed by NIR laser irradiation (1 W cm^{-2} for 1 min) if needed. The spheres were then stained with DCFH-DA (for ROS staining) and mitoTracker (for mitochondria staining) at 3, 6, and 9 h after the NIR laser irradiation. The data show ROS can be specifically produced in the mitochondria of NCI/RES-ADR sphere cells when the cells are treated with LSC or LSC-D nanoparticles and NIR laser. Without the NIR laser irradiation, the ROS production is negligible. Scale bar: 20 μm.

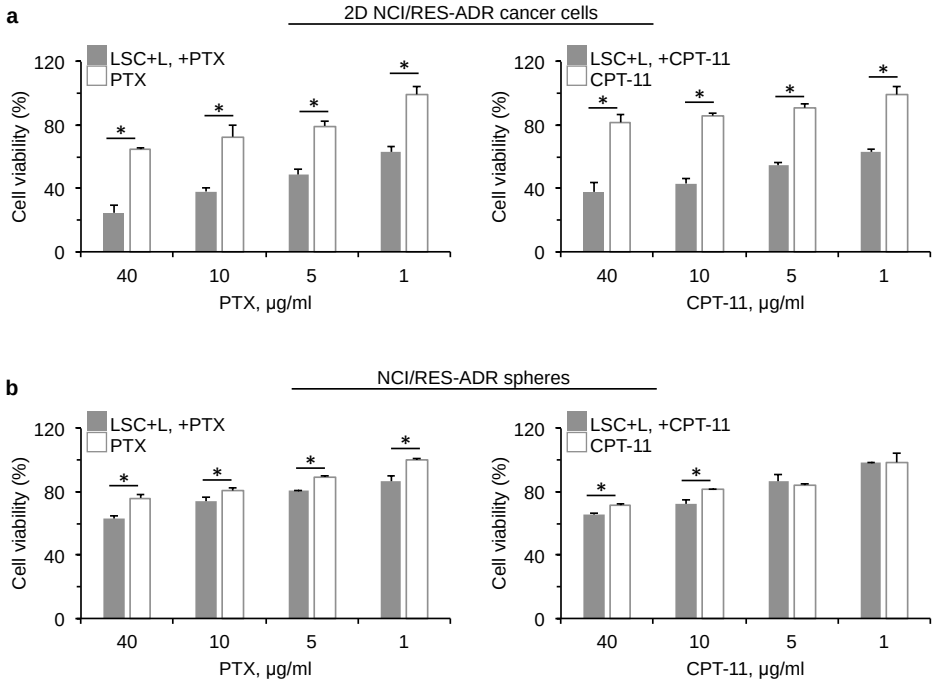

Supplementary Figure 41. The treatment of LSC nanoparticles and NIR laser irradiation sensitizes NCI/RES-ADR cells to paclitaxel and irinotecan. (**a-b**), Cytotoxicity of paclitaxel (PTX) and irinotecan (CPT-11) to 2D cultured NCI/RES-ADR cells (a) and 3D cultured NCI/RES-ADR spheres (b) without (PTX and CPT-11) or with (LSC+L, +PTX and LSC+L, +CPT11) the treatment of LSC nanoparticles and NIR laser irradiation (LSC+L). Cells were incubated with LSC nanoparticles for 12 h. After NIR laser irradiation (1 W cm^{-2} for 1 min), cells were further cultured in fresh medium containing free CPT-11 or PTX at different concentrations for 24 h. Error bars represent s.d. (n = 3). *$p < 0.05$ (Kruskal-Wallis *H*-test).

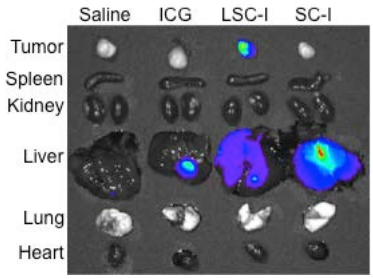

Supplementary Figure 42. Biodistribution of nanoparticles after intravenous injection. The tumor and five major organs were collected after sacrificing the mice at 6 h after intravenous injection of saline, free indocyanine green (ICG), ICG-laden LSC (LSC-I) nanoparticles, and ICG-laden SC (SC-I) nanoparticles. The data show the LSC nanoparticles can accumulate in tumor more efficiently than free ICG and SC nanoparticles.

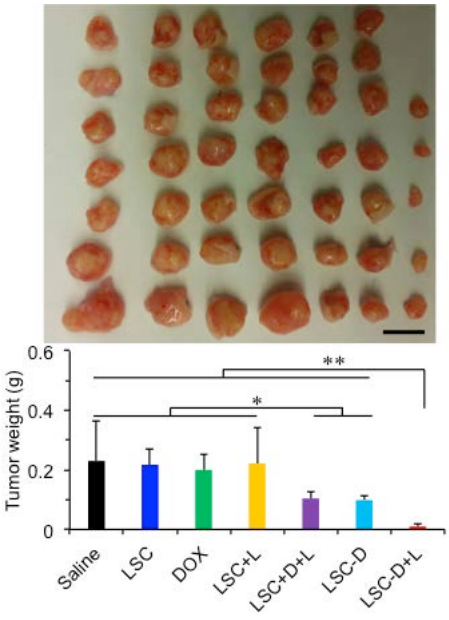

Supplementary Figure 43. Photograph and weight of the tumors collected after sacrificing the mice on day 64. The data indicate the excellent antitumor capacity of the treatment of LSC-D nanoparticles with NIR laser irradiation. Error bars represent s.d. (n = 7). $^{**}p < 0.01$, $^{*}p < 0.05$ (Kruskal-Wallis *H*-test). Scale bar: 1 cm.

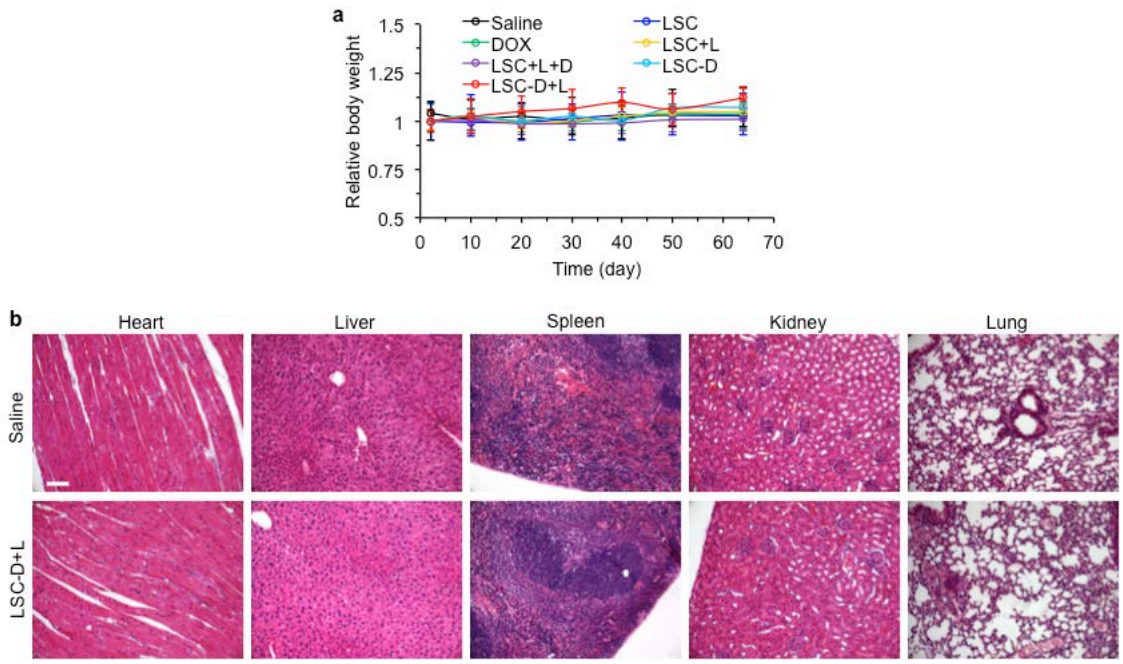

Supplementary Figure 44. No evident systemic toxicity for the treatment of LSC-D nanoparticles with NIR laser irradiation. (**a**), Body weight of mice with the various treatments showing no significant difference between the different treatments. Error bars represent s.d. (n = 7). (**b**), Representative hematoxylin & eosin (H&E) stained tissue of major organs in mice treated with saline or LSC-D nanoparticles with NIR laser irradiation (LSC-D+L). Scale bar: 150 μm.

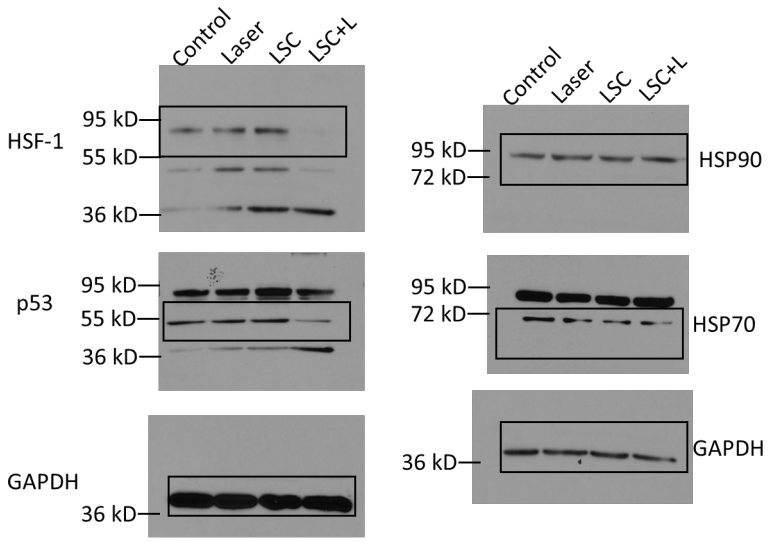

Supplementary Figure 45. Uncropped images of western blots. The boxed regions are shown in Fig. 8.

Supplementary Note 1: It is very interesting to find that the TEOS exposure can greatly shrink the CCS of ~200-300 nm and lead to the formation of SC nanoparticles of ~35 nm, representing a change in volume of ~350 times on average. The colloidal carbon sphere (CCS) is a porous material[1-3], and when it is exposed to TEOS, the TEOS may enter the porous space and react with CCS to form new chemical bonds under the experimental condition of this study. We therefore investigated the possible reaction between CCS and TEOS using proton nuclear magnetic resonance (^{1}H NMR) and Fourier transform infrared (FTIR) spectroscopy. As shown in Supplementary Fig. 4, the FTIR spectra of SC nanoparticles exhibit a unique peak at 1070 cm^{-1} (Si-O-C) compared to the spectra of CCS or pure silica nanoparticles (SiO_2), which indicates a chemical reaction between CCS and TEOS. Furthermore, peaks for both the methyl group and methylene bridge of TEOS are present in the ^{1}H NMR spectra of the SC nanoparticles, but not in the spectra of CCS and SiO_2 nanoparticles (Supplementary Fig. 5a). This further confirms that a chemical reaction between TEOS and CCS (Supplementary Fig. 5b). Therefore, there might be two events that may affect the size of the nanoparticles: (1) the formation of the new chemical bonds may generate some cohesive forces to pull the molecules in CCS closer to decrease the size of the nanoparticles, and (2) the addition of silica in the porous space and on the surface of the CCS to increase the size of the nanoparticles. It is possible that the former event dominates the latter during the first 6 h while the latter is more important than the former from 6 to 12 h, in determining the size of the nanoparticles during the process. During the synthesis of SC nanoparticles, the weight percentage of pyruvate groups in the nanoparticles decreased due to the addition of silica, while no pyruvate can be detected in pure SiO_2 nanoparticles (Supplementary Fig. 1).

Supplementary Note 2: It is worth noting that the amount of pyruvate groups in the various nanoparticles shown in Supplementary Fig. 1 is based on the same weight (50 μg) rather than the same number of the various nanoparticles. Given the same weight, the CCS content (100% for the CCS nanoparticles) in the samples of SC (-3h and -6h) and LSC nanoparticles should decrease because they also contain silica (for SC nanoparticles) and both silica and lipid (for LSC nanoparticles). This results in the decrease in the amount of the pyruvate groups in the 50 μg of SC and LSC nanoparticles. In fact, each SC or LSC nanoparticle is produced from one CCS nanoparticle, as schematically illustrated in Fig. 2a. Therefore, the total amount of pyruvate groups should be similar in each of the SC, LSC, and CCS nanoparticles. In view of this, the density of pyruvate groups on the surface of the SC and LSC nanoparticles is expected to be even higher than that on the CCS nanoparticles. This is because the size and surface area of the SC (~35 nm in diameter on average) nanoparticles are decreased by ~7 (=250/35) and ~51 (=$(250/35)^2$) times on average, respectively, compared to the CCS nanoparticles (~250 nm in diameter on average). Since LSC nanoparticles were made by coating lipid on the CS nanoparticles via its interaction with APTMS that is a silica-coupling agent (i.e., interacts with silica), the LSC and SC nanoparticles are expect to have similar density of pyruvate groups on their surface. Therefore, the addition of silica and lipid in this study should not greatly affect (and may even improve) the capability of the nanoparticles in targeting mitochondria.

Supplementary Note 3: As shown in Supplementary Fig. 9a, there is no obvious EPR signal for the DEPMPO, DEPMPO with NIR laser irradiation (DEPMPO+L), and DEPMPO mixed with LSC nanoparticles (DEPMPO+LSC). In contrast, clear signals can be detected after NIR laser irradiation of the DEPMPO+LSC (i.e., DEPMPO+LSC+L), indicating the ·OH free radicals can be produced by the LSC nanoparticles under NIR laser irradiation. This is further confirmed by using the terephthalic acid (TA) assay. TA can react with ·OH to produce 2-hydroxyterephthalic acid (2-HTA) that has a fluorescence peak at ~432 nm. Indeed, the TA solution with LSC nanoparticles after irradiated with NIR laser has stronger fluorescence than all the other control TA solutions (Supplementary Fig. 9b). Therefore, two different types of free radicals ($^1O_2$ and ·OH) or ROS can be generated by the LSC nanoparticles under NIR laser irradiation. This is probably because the CCS nanoparticles used for making the LSC nanoparticles are enriched on their surface with both sp2 and sp3 hybridized carbon atoms that could

catalyze oxidation to produce ROS (i.e., hydrogen peroxide or hydroxyl radicals)[4-6]. During NIR laser irradiation, shock photoacoustic waves could be produced to activate the carbon-steam chemical reactions on the surface of CCS nanoparticles[7,8]. Furthermore, the increase in temperature during NIR laser irradiation could also enhance the catalytic capacity of the sp2 and sp3 carbon atoms on the CCS.

Supplementary Note 4: In order to characterize and elucidate the mechanism of mitochondria targeting with our LSC nanoparticles, we prepared a lipid coated silica nanoparticle (LS) using same procedure for preparing LSC nanoparticles except that no colloidal carbon sphere (CCS) was used. As shown in Supplementary Fig. 20a, the distribution of the DOX laden-LS nanoparticles (LS-D) is different from the distribution of mitochondria, suggesting the LS nanoparticles without the colloidal carbon do not target mitochondria. To further confirm this, the intracellular distribution of LS-D nanoparticles was checked with TEM. As shown in Supplementary Fig. 21a, none of the LS nanoparticles is located in mitochondria. These results indicate that the crucial role of the CCS in rendering the LCS nanoparticles with the important property of mitochondria targeting.

Supplementary Note 5: In order to further confirm the pyruvate-mediated targeting of mitochondria with the LCS nanoparticles, we conducted more experiments to pre-treated/blocked the NCI/RES-ADR cells with pyruvic acid for 6 h before incubating them with the LSC nanoparticles. Indeed, the distribution of LSC-D nanoparticles is no longer similar to that of mitochondria according to the confocal fluorescence images (Supplementary Fig. 20b). The TEM images also show that pre-treating the cells with pyruvic acid minimizes mitochondria targeting with the LSC nanoparticles (Supplementary Fig. 21b). We further calculated the percentage of the endosome/lysosome-escaped LSC (with or without pre-blocking using pyruvic acid) or LS nanoparticles (without pre-blocking using pyruvic acid) within mitochondria. As shown in Supplementary Fig. 21c, more than 40% of the endosome/lysosome-escaped LSC-D nanoparticles are within mitochondria while it is 0% for the LS-D nanoparticles. With pre-blocking using pyruvic acid, the percentage decreases from more than 40% to ~3%. It is worth noting that to prepare cells for TEM imaging, thin slices of ~50 nm were cut through the cells. Considering the mitochondria are ~0.75-3 μm in diameter[9], the TEM images only show ~1 15^{-1}-1 60^{-1} of the whole mitochondria. As a result, only few LSC-D nanoparticles are observable in mitochondria on the TEM images and the actual number of LSC-D nanoparticles in mitochondria could be ~15-60 times of that observed in the TEM images. Taken together, these data support that the pyruvate group on the surface of the LSC nanoparticles is responsible for their capability of targeting mitochondria.

Supplementary Note 6: It is worth noting that free DOX does not target mitochondria by itself although it is a positively charged small molecule. As shown in Supplementary Figs. 12-14, free DOX does not enter the multidrug resistant NCI/RES-ADR cancer cells and it is mainly located in the nuclei of the non-drug resistant MCF-7 and OVCAR-8 cancer cells. This is further supported by the TEM data of the NCI/RES-ADR cells treated with free DOX. As shown in Supplementary Fig. 22, there is no clear difference in the cellular structure between the free DOX treated cells and the cells without any drug treatment (Fig. 3b).

Supplementary Note 7: Since the LSC-D nanoparticles are coated with DPPC on their surface, it is interesting that the nanoparticles still can target mitochondria via the pyruvate group. To clarify this, fluorescein isothiocyanate (FITC)-labeled DPPC (FITC-DPPC) is used to form the membrane coating on the LSC nanoparticles. As shown in Supplementary Fig. 23, many nanoparticles (indicated by the red fluorescence of DOX) do not overlap with the FITIC-DPPC (green), suggesting the DPPC membrane can detach from the nanoparticles after cell uptake. This is probably because the acidic environment in endo/lysosome can interrupt the binding between APTMS and DPPC formed at neutral pH during nanoparticle synthesis (Fig. 1a). This is supported by the lack of co-localization between mitochondria (purple) and FITC-DPPC while the overlap between mitochondria and nanoparticles (red) is evident (Supplementary Fig. 23). In contrast, the membrane coated on LSC-D nanoparticles is stable before cell

uptake. As shown in Supplementary Fig. 24a-c, the zeta potential of SC-D nanoparticles without lipid coating is negative (~ -41.7 mV), become positive after APTMS modification (~ 36.9), and lastly reverse to negative again after DPPC coating (~ -24.9mV). The LSC-D nanoparticles were dispersed in the cancer cell culture medium (with 10% fetal bovine serum) for 2 days and re-suspended in DI water after collected by centrifugation. Both the zeta potential and TEM image of the LSC-D nanoparticles suggest that the membrane is stably coated on the LSC-D nanoparticles (Supplementary Fig. 24d-e).

Supplementary Note 8: It is worth noting that the decreased viability of cells treated with the highest concentration of LSC nanoparticles (1.6 mg ml^{-1}) in the LSC+L group may be responsible for the decreased ATP consumption for the condition shown in Fig. 3f. This is because it is more difficult to collect all dead cells than live cells for the measurement of ATP consumption.

Supplementary Note 9: The JC-1 dye forms J-aggregates with red fluorescence at high membrane potentials, while it emits green fluorescence if the mitochondrial membrane potential is low. We incubated NCI/RES-ADR cells with LSC or LSC-D nanoparticles for 3 h, and observed the fluorescence at 3, 6, and 9 h with and without NIR irradiation. Without laser treatment, NCI/RES-ADR cells under all the conditions showed strong red fluorescence, indicating a high and intact mitochondrial membrane potential (Supplementary Fig. 29). Of note, DOX also exhibits red fluorescence resulting in a more extensive red fluorescence in LSC-D treated cells than PBS or LSC treated cells, while there is no difference among them for the green fluorescence. After NIR laser irradiation, both LSC and LSC-D treated cells exhibit much stronger green fluorescence than the cells without laser treatment, indicating a low mitochondrial membrane potential in the treated cells (Supplementary Fig. 30). The low membrane potential should be due to the decrease of the concentration gradient of protons.

Supplementary Note 10: In this study, we carefully designed our nanoparticles to compromise the important transmembrane efflux-pump mediated drug resistance mechanism of multidrug resistant cancer cells. We aim to compromise the efflux pump by minimizing the production of adenosine triphosphate (ATP) that drives the efflux pump. Therefore, first, we need to target mitochondria (the ATP factory) in the multidrug resistant cancer cells. Colloidal carbon sphere (CCS) is an important functional nanoparticle because of the rich functional groups on its surface[1-3], which could be synthesized by hydrothermally annealing glucose. Pyruvaldehyde group is one of the functional groups, which is similar to pyruvate that can specifically bind with the monocarboxylate transporters (MCTs) on the outer surface of mitochondria, for possible mitochondria targeting. Following this thought, we confirmed the existence of pyruvate in CCS by a specific detection assay first (Supplementary Fig. 1). In order to utilize the enhanced permeability and retention (EPR) of tumor vasculature for *in vivo* tumor targeting with nanoparticles of ~20-100 nm[10-12], the CCS of 200-300 nm was reacted with TEOS to form the silica-CCS (SC) hybrid nanoparticles, and further coated with lipid membrane to improve its biocompatibility and form the final LSC nanoparticle. The LSC nanoparticles are ~45 nm in diameter, which is excellent for *in vivo* tumor targeting as shown in Fig. 7a in this revision. As shown in Supplementary Fig. 1, the pyruvate groups are also detectable on the SC and LSC nanoparticles for mitochondria targeting.

References

1. Sasaki M, *et al.* Cellulose hydrolysis in subcritical and supercritical water. *J. Supercrit. Fluids* **13**, 261-268 (1998).
2. Sasaki M, Fang Z, Fukushima Y, Adschiri T, Arai K. Dissolution and hydrolysis of cellulose in subcritical and supercritical water. *Ind. Eng. Chem. Res.* **39**, 2883-2890 (2000).
3. Sevilla M, Fuertes AB. The production of carbon materials by hydrothermal carbonization of cellulose. *Carbon* **47**, 2281-2289 (2009).
4. Wang L, *et al.* Using hollow carbon nanospheres as a light-induced free radical generator to overcome chemotherapy resistance. *J. Am. Chem. Soc.* **137**, 1947-1955 (2015).

5. Chen R, Pignatello JJ. Role of quinone intermediates as electron shuttles in Fenton and photoassisted Fenton oxidations of aromatic compounds. *Environ. Sci. Technol.* **31**, 2399-2406 (1997).
6. Xu W, Dana KE, Mitch WA. Black carbon-mediated destruction of nitroglycerin and RDX by hydrogen sulfide. *Environ. Sci. Technol.* **44**, 6409-6415 (2010).
7. Chen H, Diebold G. Chemical generation of acoustic waves: a giant photoacoustic effect. *Science* **270**, 963 (1995).
8. McGrath TE, Diebold GJ, Bartels DM, Crowell RA. Laser-initiated chemical reactions in carbon suspensions. *J. Phys. Chem. A* **106**, 10072-10078 (2002).
9. Wiemerslage L, Lee D. Quantification of mitochondrial morphology in neurites of dopaminergic neurons using multiple parameters. *J. Neurosci. Methods* **262**, 56-65 (2016).
10. Kobayashi H, Watanabe R, Choyke PL. Improving conventional enhanced permeability and retention (EPR) effects: what is the appropriate target. *Theranostics* **4**, 81-89 (2013).
11. Wang H, Yu J, Lu X, He X. Nanoparticle systems reduce systemic toxicity in cancer treatment. *Nanomedicine (Lond)* **11**, 103-106 (2016).
12. Huo M, Wang L, Chen Y, Shi J. Tumor-selective catalytic nanomedicine by nanocatalyst delivery. *Nat. Commun.* **8**, 357 (2017).